Comparative study on compact quantum circuits of hybrid quantum-classical algorithms for quantum impurity models

Rihito Sakurai [1,*] Oliver J. Backhouse,[2] George H. Booth,[2] Wataru Mizukami,[3] and Hiroshi Shinaoka [1]

[1]*Department of Physics, Saitama University, Saitama 338-8570, Japan*

[2]*Department of Physics, King's College London, Strand, London WC2R 2LS, United Kingdom*

[3]*Center for Quantum Information and Quantum Biology, Osaka University, Osaka 565-0871, Japan*

(Received 8 December 2023; revised 13 February 2024; accepted 25 March 2024; published 1 May 2024)

Predicting the properties of strongly correlated materials is a significant challenge in condensed matter theory. The widely used dynamical mean-field theory faces difficulty in solving quantum impurity models numerically. Hybrid quantum-classical algorithms such as variational quantum eigensolvers emerge as a potential solution for quantum impurity models. A common challenge in these algorithms is the rapid growth of the number of variational parameters with the number of spin-orbitals in the impurity. In our approach to this problem, we develop compact *Ansätze* using a combination of two different strategies. First, we employ a compact physics-inspired *ansatz*, k-unitary cluster Jastrow *ansatz*, developed in the field of quantum chemistry. Second, we eliminate largely redundant variational parameters of physics-inspired *Ansätze* associated with bath sites based on physical intuition. This is based on the fact that a quantum impurity model with a star-like geometry has no direct hopping between bath sites. We benchmark the accuracy of these *Ansätze* for both ground-state energy and dynamic quantities by solving typical quantum impurity models with and without shot noise. The results suggest that we can maintain the accuracy of ground-state energy while we drop the number of variational parameters associated with bath sites. Furthermore, we demonstrate that a moment expansion, when combined with the proposed *Ansätze*, can calculate the imaginary-time Green's functions under the influence of shot noise. This study demonstrates the potential for addressing complex impurity models in large-scale quantum simulations with fewer variational parameters without sacrificing accuracy.

DOI: 10.1103/PhysRevResearch.6.023110

I. INTRODUCTION

Accurately predicting the properties of strongly correlated materials poses a significant challenge in condensed matter theory, including long-standing challenges in the field, such as the mechanism of high-temperature superconductivity [1,2]. Simulating these strongly correlated materials is difficult due to quantum superposition, which exponentially increases the accessible Hilbert space with the number of particles. Even with quantum computers with more than a hundred logical qubits, simulating solids with large numbers of degrees of freedom is still challenging. Quantum embedding theories, such as dynamical mean-field theory (DMFT) [3,4] or density matrix embedding theory (DMET) [5,6], aims to address this issue by limiting the correlated degrees of freedom in solid materials based on local approximation.

In DMFT, widely used in condensed matter physics, the original lattice system is divided into impurities with local interactions and an environment called a bath. This model is called a quantum impurity model. A self-consistent calculation is performed to update the parameters associated with the bath until the local Green's function defined on impurity matches that of the original lattice system with the dynamical mean field. DMFT allows us to compute the single-particle excitation spectrum and successfully describes transitions from metallic to Mott insulating behavior. The biggest numerical bottleneck in DMFT calculations is solving the correlated quantum impurity models, specifically computing local Green's functions for these interacting problems. While state-of-the-art classical algorithms have been adapted for use as impurity solvers, such as tensor networks [7–9] or quantum Monte Carlo methods [10], their applications are limited to models with only a few impurity and/or bath orbitals [7–9]. This challenge stems from the exponential increase in quantum entanglement entropy and the notorious negative sign problem.

To exploit the growing potential for solving quantum impurity models on quantum devices, quantum algorithms based on quantum phase estimation [11,12] and adiabatic algorithms [13,14] have been proposed [15]. Their practical implementation, however, may take decades because it requires large-scale error correction schemes. This led to a growing interest in variational quantum algorithms [16,17] for near-term quantum computers with limited hardware resources, often dubbed noisy intermediate-scale quantum (NISQ) devices [18]. A number of proof-of-principle

*sakurairihito@gmail.com

TABLE I. Number of variational parameters for the UCCGSD, UCCGSD(S), k-uCJ, and k-uCJ(S).

Ansatz	Number of variational parameters N_{P}
UCCGSD	$O(N_{\mathrm{SO}}^4) = O[(N_{\mathrm{imp}} + N_{\mathrm{bath}})^4]$
UCCGSD(S)	$O(N_{\mathrm{imp}}^4)$
k-uCJ	$O(N_{\mathrm{SO}}^2) = O[(N_{\mathrm{imp}} + N_{\mathrm{bath}})^2]$
k-uCJ(S)	$O(N_{\mathrm{imp}}^2)$

demonstrations of solving quantum impurity models using NISQ devices have been conducted [19–24].

In near-term quantum algorithms, such as those in the NISQ era, it is crucial to utilize limited hardware resources effectively. Therefore, there is a need to discretize a continuous bath with fewer bath sites. This reduction can be achieved through the use of imaginary time formalism in DMFT [25–29]. For example, a recent estimate for 20-orbital impurity models for iron-based superconductors indicates that about 300 bath sites are sufficient for accurate discretization in the imaginary-time formalism [27].

Once this finite Hamiltonian representation of the quantum impurity model has been found, it is now in principle amenable to solution on a quantum device. For variational quantum algorithms, the first challenge is to define an appropriate *ansatz* which is flexible enough to span the solution to the problem, able to be efficiently evaluated via unitary quantum gates, and where the number of variational parameters N_{P} does not grow prohibitively as the number of spin-orbitals N_{SO} increases. Physics-inspired *Ansätze* based on unitary coupled cluster (UCC) methods [30–32], are widely used in previous studies for quantum impurity models [23,33,34]. Among the family of UCC methods, for the unitary coupled cluster with generalized singles and doubles (UCCGSD) [35], N_{P} grows as $O(N_{\mathrm{SO}}^4)$. The computational times for computing imaginary-time Green's function grow even more rapidly, e.g., as $O(N_{\mathrm{depth}} N_{\mathrm{P}}^2)$ [36] using the UCCGSD [35] and the variational quantum simulation (VQS) [17,37], where the depth of the circuit $N_{\mathrm{depth}} \propto N_{\mathrm{P}}$. Thus, more compact *Ansätze* (circuits) are an important research direction for the success of simulating impurity models on quantum devices.

In this study, we develop compact *Ansätze* using a combination of two different strategies. First, we employ the k-unitary coupled Jastrow (k-uCJ) *ansatz* originally proposed for quantum chemistry, where N_{P} scales only as $O(N_{\mathrm{SO}}^2)$ [38]. Second, we drop largely redundant variational parameters in both the UCCGSD and the k-uCJ *ansatz* based on physical intuition. This exploits structures in the Hamiltonian which are specific to quantum impurity models with a star-like bath geometry where the bath sites are connected via the Hamiltonian only through the impurity (see Fig. 1). In particular, we eliminate part of the two-particle excitations associated with direct excitations between bath sites, which does not change the scaling of N_{P} but reduces the coefficient for a large number of bath sites. The scalings of the proposed *Ansätze* are summarized in Table I. We numerically demonstrate that the compact *Ansätze* describe ground-state energies and dynamic quantities, especially imaginary-time Green's functions, without compromising accuracy for typical quantum impurity models with or without shot noise, validating their potential in quantum impurity models.

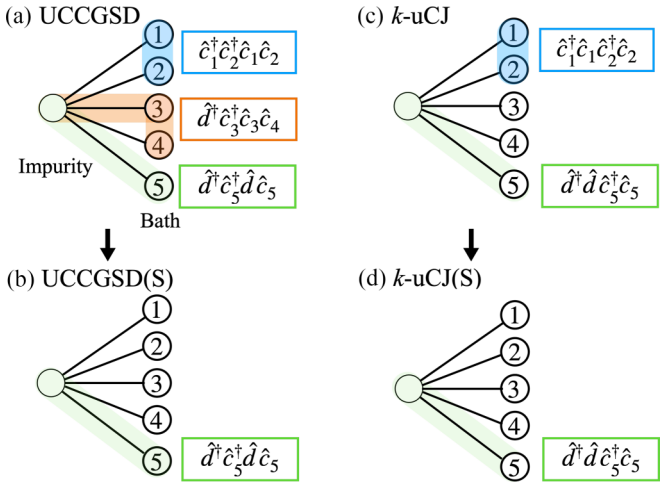

FIG. 1. Schematic illustrations for the construction of sparse *Ansätze*. (a and b) Eliminated operators that involve more than three bath orbitals when constructing the UCCGSD(S) from the UCCGSD. (c and d) Eliminated operators acting between the different bath sites when constructing the k-uCJ(S) from the k-uCJ.

The following outlines the contents of each section. Section II provides an overview of Green's functions and variational quantum algorithms for computing ground-state energy and dynamic quantities. This section also introduces the physics-inspired *Ansätze* used in this study. Section III introduces compact quantum circuits for quantum impurity models and compares the scaling of their variational parameters to those of the original *Ansätze*. Section IV compares the accuracies of ground-state energy and dynamic quantities such as spectral functions and imaginary-time Green's functions among *Ansätze* for typical quantum impurity models. Section V explores the effect of finite shot noise within the single-site impurity model. Section VI reviews our results, compares them to existing methods, and highlights areas for future research.

II. REVIEW OF GREEN'S FUNCTIONS AND VARIATIONAL QUANTUM ALGORITHMS

A. Green's function

We study a fermionic system in the grand-canonical ensemble, represented by the Hamiltonian $\mathcal{H}$, with

$$\mathcal{H} = \sum_{ij}^{N} t_{ij} \hat{c}_i^\dagger \hat{c}_j + \frac{1}{2} \sum_{ijkl} U_{ijkl} \hat{c}_i^\dagger \hat{c}_k^\dagger \hat{c}_l \hat{c}_j - \mu \sum_i \hat{c}_i^\dagger \hat{c}_i, \quad (1)$$

where $c_i / c_i^\dagger$ are annihilation and creation operators for spin-orbital i, and N represents the total number of spin-orbitals. The hopping matrix, Coulomb interaction tensor, and chemical potential are denoted by t_{ij}, U_{ijkl}, and μ, respectively. The retarded (fermionic) Green's function is defined as

$$G_{ab}^{\mathrm{R}}(t) = -\mathrm{i}\theta(t) \langle \hat{c}_a(t) \hat{c}_b^\dagger(0) + \hat{c}_b^\dagger(0) \hat{c}_a(t) \rangle, \quad (2)$$

where $\hat{c}_a(t) = e^{\mathrm{i}\mathcal{H}t} \hat{c}_a e^{-\mathrm{i}\mathcal{H}t}$ and $\hat{c}_b^\dagger(t) = e^{\mathrm{i}\mathcal{H}t} \hat{c}_b^\dagger e^{-\mathrm{i}\mathcal{H}t}$ represent the annihilation and creation operators for the spin-orbitals

a and b, respectively, in the Heisenberg representation. The $\theta(t)$ denotes the Heaviside step function. In this paper, we use $\hbar = k_B = 1$. The thermal expectation, symbolized by $\langle \cdots \rangle$, is evaluated in the grand canonical ensemble.

The retarded Green's function can be continued to the real frequency axis as

$$G^{\mathrm{R}}_{ab}(\omega) = \int_{-\infty}^{\infty} \mathrm{d}t\, e^{\mathrm{i}\omega t} G^{\mathrm{R}}_{ab}(t), \tag{3}$$

where ω is a real frequency, while the imaginary-time Green's function is defined as

$$G_{ab}(\tau) = -\theta(\tau)\langle \hat{c}_a(\tau)\hat{c}^\dagger_b(0)\rangle + \theta(-\tau)\langle \hat{c}^\dagger_b(0)\hat{c}_a(\tau)\rangle, \tag{4}$$

where $\hat{c}_a(\tau) = e^{\tau\mathcal{H}}\hat{c}_a e^{-\tau\mathcal{H}}$. Note that the imaginary-time Green's function is antiperiodic as $G_{ab}(\tau+\beta) = -G_{ab}(\tau)$. The Fourier transform of the imaginary-time Green's function, known as the Matsubara Green's function, is given by

$$G_{ab}(\mathrm{i}\omega) = \int_0^\beta \mathrm{d}\tau e^{i\omega\tau} G_{ab}(\tau), \tag{5}$$

where $\omega = (2n+1)\pi/\beta$ and $n \in \mathbb{N}$ and $\beta = 1/T$.

The Matsubara Green's function $G(i\omega)$ can be analytically continued from the imaginary axis to the full complex plane as $G_{ab}(z)$, if the spectral width is finite. The analytically continued $G_{ab}(z)$ has the spectral representation

$$G_{ab}(z) = \int_{-\infty}^{\infty} \mathrm{d}\omega \frac{A_{ab}(\omega)}{z-\omega}, \tag{6}$$

with

$$A_{ab}(\omega) \equiv \sum_{mn} (e^{-\beta E_n} + e^{-\beta E_m}) \times \langle n|\hat{c}_a|m\rangle\langle m|\hat{c}^\dagger_b|n\rangle \delta[\omega - (E_m - E_n)], \tag{7}$$

where z is a complex energy and n, m runs over all eigenstates of the system, with E_m and E_n being corresponding eigenvalues of $\mathcal{H}$. On the real axis, these eigenvalues define individual poles for a finite system, or combine to form a branch cut for an infinite system. The retarded and advanced Green's functions are given by the value of $G_{ab}(z)$ just above and below the real axis,

$$G^{\mathrm{R}}_{ab}(\omega) = G_{ab}(\omega + \mathrm{i}0^+), \tag{8}$$

$$G^{\mathrm{A}}_{ab}(\omega) = G_{ab}(\omega + \mathrm{i}0^-). \tag{9}$$

Due to the branch cut on the real axis, $G^{\mathrm{R}}_{ab}(\omega) \neq G^{\mathrm{A}}_{ab}(\omega)$ in general. The following relationship holds between the spectral function and the retarded and advanced Green's functions:

$$A_{ab}(\omega) = -\frac{1}{2\pi\mathrm{i}}\left[G^{\mathrm{R}}_{ab}(\omega) - G^{\mathrm{A}}_{ab}(\omega)\right], \tag{10}$$

where we used the formula $1/(x+\mathrm{i}0^+) = \mathcal{P}(1/x) - \mathrm{i}\pi\delta(x)$, and $\mathcal{P}$ stands for the principal value.

We now consider the limit of $T \to 0$, where the ensemble average is restricted to the ground state(s) Ψ_{G}. At sufficiently low temperatures, Eq. (4) can be rewritten as

$$G_{ab}(\tau) \underset{T\to 0}{=} \mp\langle\Psi_{\mathrm{G}}|\hat{A}_\pm e^{\mp(\mathcal{H}-E_{\mathrm{G}})\tau}\hat{B}_\pm|\Psi_{\mathrm{G}}\rangle, \tag{11}$$

where $A_+ = \hat{c}_a$ and $B_+ = \hat{c}^\dagger_b$ for $0 < \tau < \beta/2$, and $A_- = \hat{c}^\dagger_b$ and $B_- = \hat{c}_a$ for $-\beta/2 < \tau < 0$. The signs $\mp$ are for $\tau > 0$ and $\tau < 0$, respectively, and $E_{\mathrm{G}} = \langle\Psi_{\mathrm{G}}|\mathcal{H}|\Psi_{\mathrm{G}}\rangle$. In the presence of degenerate ground states, Eq. (11) should be averaged over all such states. In general, $|G_{ab}(\tau)|$ decays exponentially in an insulating system, while algebraic in a metallic system. In numerical simulations, one sometimes uses the finite-temperature formalism with a sufficiently large β. To ensure that $G_{ab}(\tau)$ is sufficiently small at the boundary, we need to increase β, which determines the upper limit of time evolution.

B. Variational quantum algorithms

In quantum computing, it is necessary to convert fermionic operators into qubit representations. There are several methods for this, such as the Jordan-Wigner transformation [39] and the Bravyi-Kitaev transformation [40,41]. In this study, we use the Jordan-Wigner transformation given by

$$\hat{c}^\dagger_j \to \tfrac{1}{2}(X_j - iY_j)Z_1Z_2\ldots Z_{j-1}, \tag{12}$$

$$\hat{c}_j \to \tfrac{1}{2}(X_j + iY_j)Z_1Z_2\ldots Z_{j-1}. \tag{13}$$

1. Ground-state calculation using variational quantum eigensolver

We use a variational quantum eigensolver (VQE) [16,42]. It begins by preparing an initial state $|\Psi_{\mathrm{init}}\rangle$ on a quantum computer. Then, a unitary operator described by a parametrized circuit with variational parameters $\boldsymbol{\theta}$, denoted as $U(\boldsymbol{\theta})$, is applied to the initial state, producing a quantum state $|\Psi(\boldsymbol{\theta})\rangle$. Subsequently, the expectation value of each term in the Hamiltonian is measured using the quantum computer. This measured data is accumulated to compute the total expectation value of the Hamiltonian $\langle\mathcal{H}\rangle$ on a classical computer. The variational parameters are updated on the classical computer to minimize $\langle\mathcal{H}\rangle$, and the process is iterated until the parameters are stably minimized. Provided the *ansatz* has sufficiently high expressive power and the optimization is carried out well using an appropriate initial state, the variational quantum state $|\Psi(\boldsymbol{\theta}^*)\rangle$ with optimized variational parameters $\boldsymbol{\theta}^*$ approximates the ground state $|\Psi_{\mathrm{G}}\rangle$ accurately. The success of the VQE therefore relies on finding an appropriate representation of the quantum state in terms of a sufficiently compact parametric quantum circuit that can be optimized classically.

2. Recursive VQE for spectral moments

We detail here an approach to extend the scope of VQE to optimize the dynamics of the single-particle excitation spectrum via a compact moment expansion. This expansion allows access to a causal imaginary-time Green's function directly at zero temperature and in a fashion that allows for efficient quantum computation via a modified VQE [43–45]. In a recent paper, direct measurements of the moment expansion expectation values via VQE have been proposed to compute the Green's functions [22]. However, the proposed approach required measuring an increasing number of Pauli terms at higher-order moments and as systems increase in size, which we aim to mitigate via a recursive VQE approach to avoid this issue, as we will detail below.

The key physical quantities we aim to compute on the quantum device are the spectral moments of the Green's function. This quantity, which is classified as either hole or particle type at zero temperature, is defined in each case at the order m as follows:

$$M_{rs}^{\mathrm{h},(m)} = \langle \Psi_{\mathrm{G}} | \hat{c}_r^\dagger [\mathcal{H}_{\mathcal{N}}]^m \hat{c}_s | \Psi_{\mathrm{G}} \rangle, \tag{14}$$

$$M_{rs}^{\mathrm{p},(m)} = \langle \Psi_{\mathrm{G}} | \hat{c}_r [\mathcal{H}_{\mathcal{N}}]^m \hat{c}_s^\dagger | \Psi_{\mathrm{G}} \rangle, \tag{15}$$

where $\mathcal{H}_{\mathcal{N}} = \mathcal{H} - E_{\mathrm{G}}$.

These can be related to the matrix-valued spectral function $A(\omega)_{rs}$, defined in Eq. (10), as

$$M_{rs}^{\mathrm{h},(m)} = \int_{-\infty}^{0} A_{rs}(\omega) \omega^m \mathrm{d}\omega, \tag{16}$$

$$M_{rs}^{\mathrm{p},(m)} = \int_{0}^{\infty} A_{rs}(\omega) \omega^m \mathrm{d}\omega. \tag{17}$$

The spectral moments defined in Eqs. (14) and (15) correspond to the Taylor expansions of the imaginary-time Green's function at the discontinuity points $\tau = 0^-$ and $\tau = 0^+$, respectively. By increasing the number of moments, the imaginary-time Green's function can be systematically approximated over longer times τ.

Once the spectral moments for the particle and hole sectors are determined up to a maximum order N_{mom}, we can appeal to the block Lanczos algorithm [46] to constructively build an effective single-particle Hamiltonian from these moments. This single-particle Hamiltonian spans the physical system and couples to it an auxiliary system whose dimensionality grows linearly with the number of system degrees of freedom and the maximum order N_{mom}. This auxiliary system acts as a zero-temperature dynamical self-energy, allowing correlation-driven changes to the original spectrum. These changes result from the projection of the eigenstates of this effective Hamiltonian back into the physical system. This auxiliary space is built in such a way that the resulting spectrum is causal, obeys required sum rules, and exactly preserves the initially provided moments, according to Eqs. (16) and (17). The resulting Green's function can be obtained directly in the Lehmann representation from the diagonalization of this effective Hamiltonian, providing the residues and energies of all the poles and allowing the Green's function to be easily transformed into any domain, including imaginary time. For more details of this procedure, see Refs. [[43–45]], while similar approaches have also recently been applied in classical perturbative electronic structure methods to expand the self-energy [47,48].

We describe the procedure for calculating the moments defined by Eqs. (14) and (15) using a hybrid quantum-classical optimization algorithm, similar to the VQE approach for the ground state. We assume that approximated $|\Psi_{\mathrm{G}}\rangle$ and E_{G} are already computed using VQE. To simplify the exposition, we describe the construction of the particle sector moments, with the hole moments computed analogously.

First, we prepare a variational quantum state for the single-particle excited state $\hat{c}_s^\dagger |\Psi_{\mathrm{G}}\rangle$. Because the operator is not unitary, we represent the resultant state as the action of a unitary multiplied by a scalar as

$$\hat{c}_s^\dagger |\Psi_{\mathrm{G}}\rangle \simeq d_0 \left| \phi_{\mathrm{EX}}^0 \left(\boldsymbol{\theta}_{\mathrm{EX}}^0 \right) \right\rangle, \tag{18}$$

where d_0 is a coefficient and the parametrized quantum state $|\phi_{\mathrm{EX}}(\boldsymbol{\theta}_{\mathrm{EX}}^0)\rangle$ is defined by

$$\left| \phi_{\mathrm{EX}}^0 \left(\boldsymbol{\theta}_{\mathrm{EX}}^0 \right) \right\rangle = U \left(\boldsymbol{\theta}_{\mathrm{EX}}^0 \right) \left| \phi_{\mathrm{EX}}^0 \right\rangle. \tag{19}$$

We choose to construct this state by defining an initial state $|\phi_{\mathrm{EX}}^0\rangle$ with $N+1$ electrons and ensure that our parametrization for $U(\boldsymbol{\theta}_{\mathrm{EX}}^0)$ conserves the electron number of the state.

The variational parameters $\boldsymbol{\theta}_{\mathrm{EX}}^0$ and coefficient d_0 can be computed as follows: After transforming $\hat{c}_s^\dagger$ into the qubit representation, we measure the cost function defined by

$$C = -\left| \left\langle \phi_{\mathrm{EX}}^0 \left(\boldsymbol{\theta}_{\mathrm{EX}}^0 \right) \right| \hat{c}_s^\dagger | \Psi_{\mathrm{G}} \rangle \right|^2. \tag{20}$$

We evaluate Eq. (20) on the quantum computer via a circuit similar to a Hadamard test [49,50] (see Appendix A). The variational parameters are optimized to minimize the cost function C until convergence is achieved. After this optimization process, the scaling coefficient, defined as follows, is measured on the quantum device:

$$d_0 = \left\langle \phi_{\mathrm{EX}}^0 \left(\boldsymbol{\theta}_{\mathrm{EX}}^{0*} \right) \right| \hat{c}_s^\dagger | \Psi_{\mathrm{G}} \rangle. \tag{21}$$

Finally, the zeroth-order moment, defined as follows, can be computed via sampling:

$$M_{rs}^{\mathrm{p},(0)} = \langle \Psi_{\mathrm{G}} | \hat{c}_r \hat{c}_s^\dagger | \Psi_{\mathrm{G}} \rangle \approx d_0 \langle \Psi_{\mathrm{G}} | \hat{c}_r \left| \phi_{\mathrm{EX}}^0 \left(\boldsymbol{\theta}_{\mathrm{EX}}^{0*} \right) \right\rangle. \tag{22}$$

We can then subsequently compute the higher-order moments up to the maximum order of the moments order with $(1 \leqslant m \leqslant N_{\mathrm{mom}})$ via a recursive approach, avoiding the need to measure over increasingly large numbers of Pauli strings for higher-order moments, as considered in Ref. [22]. Using $|\phi_{\mathrm{EX}}^{(m-1)}(\boldsymbol{\theta}_{\mathrm{EX}}^{(m-1)*})\rangle$ computed in the previous step, we approximate $\mathcal{H}_{\mathcal{N}} |\phi_{\mathrm{EX}}^{(m-1)}(\boldsymbol{\theta}_{\mathrm{EX}}^{(m-1)*})\rangle$ as

$$\mathcal{H}_{\mathcal{N}} \left| \phi_{\mathrm{EX}}^{(m-1)} \left(\boldsymbol{\theta}_{\mathrm{EX}}^{(m-1)*} \right) \right\rangle \simeq d_m \left| \phi_{\mathrm{EX}}^{m} \left(\boldsymbol{\theta}_{\mathrm{EX}}^{m} \right) \right\rangle. \tag{23}$$

The variational parameters $\boldsymbol{\theta}_{\mathrm{EX}}^m$ and constant coefficient d_m are determined by minimizing the following cost function:

$$C = -\left| \left\langle \phi_{\mathrm{EX}}^{m} \left(\boldsymbol{\theta}_{\mathrm{EX}}^{m} \right) \right| \mathcal{H}_{\mathcal{N}} \left| \phi_{\mathrm{EX}}^{(m-1)} \left(\boldsymbol{\theta}_{\mathrm{EX}}^{(m-1)} \right) \right\rangle \right|^2. \tag{24}$$

By performing m VQE steps optimizing these states, we can calculate the moments of order m as

$$\begin{aligned} M_{rs}^{\mathrm{p},(m)} &= \langle \Psi | \hat{c}_r [\mathcal{H}_{\mathcal{N}}]^m \hat{c}_s^\dagger | \Psi \rangle \\ &= d_0 d_1 \ldots d_m \langle \Psi_{\mathrm{G}} | \hat{c}_r \left| \phi_{\mathrm{EX}}^{m} \left(\boldsymbol{\theta}_{\mathrm{EX}}^{m*} \right) \right\rangle. \end{aligned} \tag{25}$$

Similar ideas of hybrid quantum-classical variational optimization of alternative functionals for computing other (e.g., dynamical) properties have also been considered in other works [17,49,51–54].

As the *ansatz* used in optimizing all m states $|\phi_{\mathrm{EX}}^m(\boldsymbol{\theta}_{\mathrm{EX}}^m)\rangle$ becomes complete, it should enable the computation of the *exact* moments up to order m using the described approach. However, this optimization is also subject to various types of noises, including finite sampling errors of expectation values in a physical device, as well as optimization bottlenecks. This can result in numerical errors, which would likely accumulate exponentially at high orders of m. Nevertheless, as the magnitude of the moment also increases exponentially with respect to its order, we find that the numerical relative error in these moments compared to their exact benchmarks remains almost constant (see Appendix B). Finally, we note that while this

approach has been presented for the computation of single-site Green's functions and moments, off-diagonal elements corresponding to matrix-valued Green's functions are possible, analogous to the approaches in Refs. [49] and [22].

C. *Ansätze*

We use two physics-inspired *Ansätze*: UCCGSD [35,55] and *k*-uCJ [38], which we describe below.

1. *UCCGSD*

The UCCGSD is a generalization of a unitary coupled cluster (UCC) [30,31,56–59] written as the exponential of an antisymmetric sum of excitation operators. The UCCGSD is formulated as follows:

$$|\Psi_{\mathrm{UCCGSD}}\rangle = e^{(\hat{T}_2-\hat{T}_2^\dagger)+(\hat{T}_1-\hat{T}_1^\dagger)}|\Psi_{\mathrm{init}}\rangle, \tag{26}$$

where $|\Psi_{\mathrm{init}}\rangle$ represents an initial product state, while $\hat{T}_n$ ($n = 1, 2$) and their respective conjugates $\hat{T}_n^\dagger$ are excitation operators. The excitation operators $\hat{T}_n$ are given by

$$\hat{T}_1 = \sum_{pq,\alpha\beta} t_{pq}^{\alpha\beta}\hat{c}_{p\alpha}^\dagger\hat{c}_{q\beta}, \tag{27}$$

$$\hat{T}_2 = \frac{1}{4}\sum_{pqrs,\alpha\beta\gamma\zeta} t_{pqrs}^{\alpha\beta\gamma\zeta}\hat{c}_{p\alpha}^\dagger\hat{c}_{q\beta}^\dagger\hat{c}_{r\gamma}\hat{c}_{s\zeta}, \tag{28}$$

where $\hat{T}_1$ is a single-particle excitation operator, and $\hat{T}_2$ is a two-particle excitation operator. The indices p, q, r, s represent spatial orbitals, and $\alpha, \beta, \gamma, \zeta$ represent spin. The composite indices $p\alpha, q\beta, r\gamma, s\zeta$ span all spin-orbitals N_{SO}. In this study, we removed one-particle and two-particle excitations that change total S_z. The $t_{pq}^{\alpha\beta}$ and $t_{pqrs}^{\alpha\beta\gamma\zeta}$ are complex-number variational parameters. The number of variational parameters N_{P} scales as $O(N_{\mathrm{SO}}^4) = O[(N_{\mathrm{imp}} + N_{\mathrm{bath}})^4]$, where N_{imp} represents the number of spin-orbitals of the impurity and N_{bath} the number in the bath.

Computing $\langle\Psi_{\mathrm{UCCGSD}}|\mathcal{H}|\Psi_{\mathrm{UCCGSD}}\rangle$ is exponentially expensive on classical computers because it results in a nontruncating Baker-Campbell-Hausdorff expansion. In contrast, quantum computers can compute this expectation value directly. We use a Trotter decomposition to implement Eq. (26) on a quantum computer. Classical optimization of variational quantum algorithms can partially mitigate the Trotterization error [60,61], but does result in a dependence of the final state on the ordering of the individual excitation operators. As commonly done, we set the Trotter step to 1, resulting in

$$\begin{aligned}
|\Psi_{\mathrm{UCCGSD}}\rangle &\simeq e^{(\hat{T}_2-\hat{T}_2^\dagger)}e^{(\hat{T}_1-\hat{T}_1^\dagger)}|\Psi_{\mathrm{init}}\rangle \\
&= \prod_{p\alpha,q\beta,r\gamma,s\zeta}^{N_{\mathrm{SO}}}\left\{e^{t_{\alpha\beta\gamma\zeta}^{pqrs}\hat{c}_{p\alpha}^\dagger\hat{c}_{q\beta}^\dagger c_{r\gamma}c_{s\zeta} - t_{\alpha\beta\gamma\zeta}^{pqrs*}\hat{c}_{s\zeta}^\dagger\hat{c}_{r\gamma}^\dagger\hat{c}_{q\beta}\hat{c}_{p\alpha}}\right\} \\
&\quad\times\prod_{p\alpha,q\beta}^{N_{\mathrm{SO}}}\left\{e^{t_{pq}^{\alpha\beta}\hat{c}_{p\alpha}^\dagger\hat{c}_{q\beta} - t_{pq}^{\alpha\beta*}\hat{c}_{q\beta}^\dagger\hat{c}_{p\alpha}}\right\}|\Psi_{\mathrm{init}}\rangle \\
&= \prod_{p\alpha,q\beta,r\gamma,s\zeta}^{N_{\mathrm{SO}}}\left\{e^{t_{\alpha\beta\gamma\zeta}^{pqrs}\hat{c}_{p\alpha}^\dagger\hat{c}_{q\beta}^\dagger c_{r\gamma}c_{s\zeta} - t_{\alpha\beta\gamma\zeta}^{pqrs*}\hat{c}_{s\zeta}^\dagger\hat{c}_{r\gamma}^\dagger\hat{c}_{q\beta}\hat{c}_{p\alpha}}\right\}|\Psi_{\mathrm{orb}}\rangle,
\end{aligned} \tag{29}$$

where $|\Psi_{\mathrm{orb}}\rangle \equiv \prod_{p\alpha,q\beta}^{N_{\mathrm{SO}}}\{e^{t_{pq}^{\alpha\beta}\hat{c}_{p\alpha}^\dagger\hat{c}_{q\beta} - t_{pq}^{\alpha\beta*}\hat{c}_{q\beta}^\dagger\hat{c}_{p\alpha}}\}|\Psi_{\mathrm{init}}\rangle$, demonstrating that the UCCGSD *ansatz* incorporates single-particle basis rotations into its definition [62].

2. *k-uCJ*

Let us first define the unitary cluster Jastrow (uCJ) *ansatz* and then the *k*-uCJ *ansatz* [38]. The uCJ *ansatz* is defined as follows:

$$|\Psi_{\mathrm{uCJ}}\rangle = e^{\hat{K}}e^{\hat{J}}e^{-\hat{K}}|\Psi_{\mathrm{orb}}\rangle, \tag{30}$$

where

$$\hat{K} = \sum_{pq,\alpha}\mathcal{K}_{pq}\hat{c}_{q\alpha}^\dagger\hat{c}_{p\alpha}, \tag{31}$$

$$\hat{J} = \sum_{pq,\alpha\beta}\mathcal{J}_{pq}^{\alpha\beta}\hat{c}_{p\alpha}^\dagger\hat{c}_{p\alpha}\hat{c}_{q\beta}^\dagger\hat{c}_{q\beta}. \tag{32}$$

The matrix $\mathcal{K}$ is complex and anti-Hermitian. The matrix $\mathcal{J}$ is symmetric, and its elements are purely imaginary. The $|\Psi_{\mathrm{orb}}\rangle$ is the single-particle basis rotated state defined in Eq. (29). This *ansatz* preserves the particle's number and total S_z. The scaling with N_{P} is $O(N_{\mathrm{SO}}^2) = O[(N_{\mathrm{imp}} + N_{\mathrm{bath}})^2]$.

The uCJ *ansatz* is motivated via a tensor decomposition process that compresses the generalized two-particle excitation operators in the coupled cluster method. This *ansatz* compresses two-particle excitation operators into number operators with just two indices $(p\alpha)$ and $(q\beta)$. This reduces the number of the variational parameters, for instance, compared to UCCGSD. Similar approaches based on tensor decomposition have been proposed in Refs. [63–67]. Equation (32) can be implemented without Trotterization, as it involves only commuting number operators. By performing the Jordan-Wigner transformation on the equation, this term $\hat{c}_{p\alpha}^\dagger\hat{c}_{p\alpha}\hat{c}_{q\beta}^\dagger\hat{c}_{q\beta}$ can be simplified to $\frac{1}{4}(1 - Z_{p\alpha})(1 - Z_{q\beta})$. The *k*-uCJ *ansatz* differs from the uCJ *ansatz* in that the operators $\mathcal{J}$ and $\mathcal{K}$ are applied multiple times, resulting in the *k*-uCJ *ansatz*,

$$|\Psi_{k\text{-uCJ}}\rangle = \prod_{i=1}^{k} e^{\hat{K}_i}e^{\hat{J}_i}e^{-\hat{K}_i}|\Psi_{\mathrm{orb}}\rangle, \tag{33}$$

where variational parameters for different i are independently optimized. The *k*-uCJ *ansatz* becomes more accurate as k is increased.

III. SPARSE *Ansätze*

In a quantum embedding calculation, a continuous hybridization can be discretized with a finite number of bath sites. In particular, for a star-like geometry, the bath sites are connected only through the impurity. The number of bath sites N_{bath} required for an accurate discretization scales linearly with N_{imp}, albeit with a significant prefactor (on the order of ten [27]). Given the significant number of variational parameters associated with the bath sites, reducing the number of these parameters is critical for efficient quantum simulation of impurity models.

We propose compact *Ansätze* for quantum impurity models with star-like bath geometries. We assume that two-particle excitation operators associated with two-body coupling between bath sites are not critical in the description of the ground

states and spectral moments, given that two-particle interaction terms in the Hamiltonian are localized to the impurity space, and no Hamiltonian terms directly couple the bath sites. The *Ansätze* incorporating this assumption are referred to as "sparse *Ansätze*." In the present study, we construct sparse *Ansätze* based on the UCCGSD and the k-uCJ. We call them sparse UCCGSD and sparse k-uCJ, denoted UCCGSD(S) and k-uCJ(S), respectively.

For the UCCGSD, we remove two-particle excitation operators that involve more than three bath orbitals. Examples of such operators that involve three or four bath orbitals are $\hat{c}_1^\dagger \hat{c}_1^\dagger \hat{c}_2 \hat{c}_2$ and $\hat{d}^\dagger \hat{c}_3^\dagger \hat{c}_3 \hat{c}_4$, where $\hat{d}^\dagger$ ($\hat{c}^\dagger$) are fermionic creation operators for the impurity (bath) degrees of freedom, respectively. We illustrate these operators in Figs. 1(a) and 1(b). For the UCCGSD, this reduces the number of variational parameters N_P from $O[(N_\mathrm{imp}+N_\mathrm{bath})^4]$ to $O(N_\mathrm{imp}^4 + N_\mathrm{bath}^2) \simeq O(N_\mathrm{imp}^4)$ for the sparse variant (refer to Table I). Although N_bath is proportional to N_imp [27], ensuring that the scaling with respect to impurity size remains the same, the significant computational savings still result since $N_\mathrm{bath} \gg N_\mathrm{imp}$.

For the k-uCJ, we apply a similar motivation to remove the operators acting between different bath sites while keeping the two-particle excitation operators between the impurity and the bath. For example, $\hat{c}_1^\dagger \hat{c}_1 \hat{c}_2^\dagger \hat{c}_2$ is dropped, as illustrated in Figs. 1(c) and 1(d). As summarized in Table I, the scaling of N_P in the k-uCJ *ansatz* scales as $O[(N_\mathrm{imp}+N_\mathrm{bath})^2]$, while N_P in the corresponding k-uCJ(S) sparse *ansatz* scales as $O(N_\mathrm{imp}^2)$. Again, the prefactor is substantially reduced when $N_\mathrm{bath} \gg N_\mathrm{imp}$.

In the case of sparse *Ansätze*, reducing the number of two-particle excitation operators will lead to a reduction in the number of CNOT gates. The number of reduced CNOT gates is proportional to the number of reduced terms in the two-particle excitation operators.

IV. STATE VECTOR SIMULATION

In this section, we benchmark the k-uCJ and the proposed sparse *Ansätze* for typical quantum impurity models. We consider both single-site and two-site impurity models with $N_\mathrm{bath} = 3$ and $N_\mathrm{bath} = 6$, respectively. All calculations in this section are based on state vector simulations of quantum circuits.

A. Numerical details

The calculations were performed using the following libraries: QCMATERIALNEW [68] was used as a quantum circuit simulator, which is a Julia wrapper of QULACS [69]. We used OPENFERMION [70] for the Jordan-Wigner transformation and to calculate the exact eigenvalues of Hamiltonians. We performed DMFT calculations using DCORE [71] to generate the single-site impurity models. We used the DYSON [72] library in order to compute the Green's functions poles and residues from the spectral moments, as well as benchmark exact spectral moments via exact diagonalization.

To optimize the variational parameters, we used the Broyden-Fletcher-Goldfarb-Shanno (BFGS) algorithm. In this study, we employ the numerical finite difference method for gradient calculation, setting the value of the finite difference to 10^{-5}. We observed that setting the initial guess to zero could lead the optimization to converge to a metastable solution. We initialized the variational parameters with random numbers, although this approach does not entirely eliminate the possibility of being trapped in a metastable solution. For ground-state calculations with VQE using the k-uCJ, we increased the number of terms k in the *ansatz* one by one, reusing the optimized variational parameters. In practice, at the beginning of the VQE calculations with k terms, we randomized the variational parameters in $\hat{K}_1$ and $\hat{J}_1$ but set those in $\hat{K}_i$ and $\hat{J}_i$ ($2 \leqslant i \leqslant k$) to the optimized variational parameters obtained in the previous calculation with $k-1$ terms. This procedure ensures that the optimized energy decreases or remains nearly stable with an increasing number of terms in the k-uCJ. While it was not attempted in this study, there is a possibility that further optimization could be achieved by conducting a complete reoptimization of all the k terms of k-uCJ simultaneously after optimizing the kth terms.

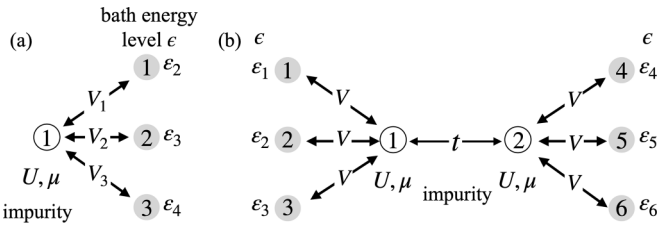

FIG. 2. Two quantum impurity models used in this study. (a) Single-site impurity model with $N_\mathrm{bath} = 3$ and (b) two-site impurity model with $N_\mathrm{bath} = 6$.

For convergence in energy and spectral moments, we conducted 1000 BFGS iterations for the single-site impurity model (see Secs. IV B and V A) and 300 iterations for the two-site impurity model (see Sec. IV C 1). Additionally, to demonstrate the dependence of the initial parameters on the ground-state energy, the number of initial guesses was set to 50 for the single-site impurity model (see Figs. IV B 1 and V A) and 20 for the two-site impurity model (see Fig. IV C 1).

It is worth noting that the initial parameters significantly influence the accuracy of the optimized ground state and spectral moments. For ground-state calculations, we conducted VQE multiple times, each with a different set of initial parameters, to find the best variational state for the ground state. We used this best variational state for computing spectral moments.

Simulations were executed using an Message Passing Interface (MPI) parallelized program on a workstation with an AMD EPYC 7702P 64-core processor. Solving the largest model with 16 qubits and about 750 variational parameters in the k-uCJ took about 5 days on 55 cores using VQE and the recursive approach.

B. Single-site impurity model

We consider the single-site impurity model with particle-hole symmetry and $N_\mathrm{bath} = 3$ illustrated in Fig. 2(a). The number of qubits in this model is 8. The Hamiltonian is given

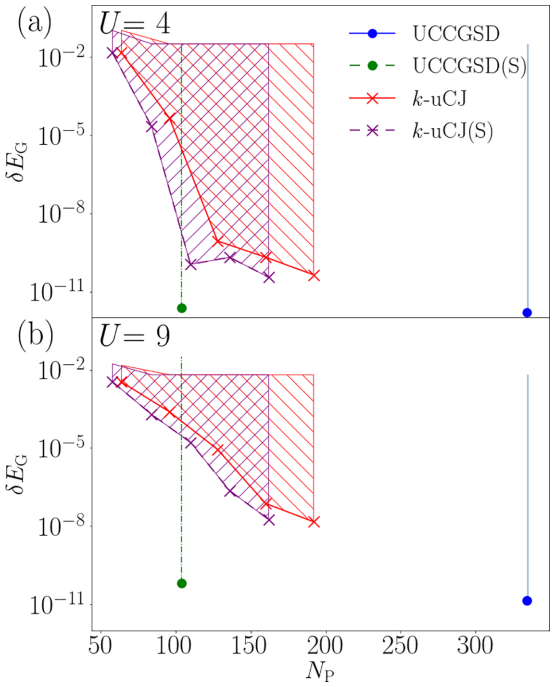

FIG. 3. Computed δE_{G} for the single-site impurity model, where the x axis represents the number of parameters N_{P}. (a and b) Results for $U = 4$ and $U = 9$, respectively. In the k-uCJ and the k-uCJ(S), k increases from 1 to 5. The markers represent the smallest errors when the initial parameters are changed 50 times. The hatched lines in the figures show how absolute errors depend on initial parameters for k-uCJ and k-uCJ(S), respectively. The vertical lines indicate similar dependency for UCCGSD and UCCGSD(S), respectively.

by

$$\mathcal{H} = U\hat{d}^{\dagger}_{1\uparrow}\hat{d}_{1\uparrow}\hat{d}^{\dagger}_{1\downarrow}\hat{d}_{1\downarrow} - \mu \sum_{\sigma=\uparrow,\downarrow} \hat{d}^{\dagger}_{1\sigma}\hat{d}_{1\sigma} - \sum_{k=1}^{3}\sum_{\sigma=\uparrow,\downarrow} V_k(\hat{d}^{\dagger}_{1\sigma}\hat{c}_{k\sigma} + \hat{c}^{\dagger}_{k\sigma}\hat{d}_{1\sigma}) + \sum_{k=1}^{3}\sum_{\sigma=\uparrow,\downarrow} \epsilon_k \hat{c}^{\dagger}_{k\sigma}\hat{c}_{k\sigma}, \tag{34}$$

where $\hat{d}^{\dagger}_{1\sigma}$ ($\hat{c}^{\dagger}_{k\sigma}$) are the impurity (bath) degrees of freedom of the fermionic creation operator with $\sigma = \uparrow, \downarrow$, and k is an index for bath sites. The U represents the on-site Coulomb repulsion, V_k is the hybridization term, $\mu\,(= U/2)$ is the chemical potential, and ϵ_k denotes the bath energy.

We obtained the bath parameters using self-consistent DMFT calculations on a square lattice at zero temperature for $U = 4$ (metallic phase) and $U = 9$ (insulating phase). The nearest-neighbor hopping parameter was set to 1. For $U = 4$, we obtained $V_k = \{-1.26264, 0.07702, -1.26264\}$ and $\epsilon_k = \{1.11919, 0.0, -1.11919\}$. For $U = 9$, we obtained $V_k = \{1.31098, 0.07658, -1.38519\}$ and $\epsilon_k = \{-3.26141, 0.0, 3.26141\}$.

1. Ground-state calculation

Figures 3(a) and 3(b) show the absolute errors in ground-state energies (δE_{G}) for $U = 4$ and $U = 9$, respectively, compared to exact diagonalization results. For the k-uCJ and the k-uCJ(S), we varied k from 1 to 5 to check convergence. The markers represent the best results obtained by varying the initial parameters 50 times for each *ansatz*. The hatched lines indicate the variation in converged results depending on the choice of initial parameters for each *ansatz*. In all four *Ansätze*, the best ground-state energies are well reproduced. We also confirmed that the k-uCJ reproduces the ground-state energy with smaller N_{P} than the UCCGSD. Also, the results for the sparse *Ansätze* in Figs. 3(a) and 3(b) show that reducing the variational parameters associated with bath sites does not compromise the accuracy of the ground-state energies. Also, the sparse k-uCJ with fewer parameters results in smaller errors than those of k-uCJ. One possible explanation is that reducing the number of parameters in the sparse *ansatz* simplifies the landscape of the cost functions, making it easier for the optimization algorithm to find a more accurate solution. It should be noted that the sparse *Ansätze* are efficient even for the metal-like system ($U = 4$), where the electronic structure is very much delocalized across the bath sites.

The following summarizes the reduction in N_{P} for each *ansatz* by using the sparseness. In the UCCGSD, N_{P} is reduced from 334 to 104. In the k-uCJ, N_{P} is reduced from $\{64, 96, 128, 160, 192\}$ to $\{58, 84, 110, 136, 162\}$ for $k = 1, 2, \ldots, 5$. The k-uCJ(S) has a small reduction in the number of parameters for this system, but this reduction becomes more significant with increasing system size and complexity (see Sec. IV C 1).

2. Spectral functions

Figures 4(a) and 4(b) show the reconstructed spectral functions using the moment expansion for $U = 4$ and $U = 9$, respectively. For the k-uCJ, we set $k = 5$. We computed the exact values of the moments using exact diagonalization (ED). As shown in Fig. 4(a), for $U = 4$, all the *Ansätze* can reproduce the peaks around $\omega = 0$. However, the quality of reproduction drops for $\omega \geqslant 2$. These discrepancies primarily arise from numerical errors during the moment computations via recursive VQE due to the limited representational ability of the *Ansätze* and the optimization issues. This *fitting error* in the recursive approach grows exponentially with the maximum order N_{mom}, which prevents systematic improvement of reconstructed spectral functions with increasing N_{mom}. Indeed, we observed no improvement for $N_{\mathrm{mom}} > 7$, although knowledge of the exact moments up to order $N_{\mathrm{mom}} = 5$ is largely sufficient to converge the spectral function over all frequencies.

As shown in Fig. 4(b), for $U = 9$, by increasing the maximum order N_{mom} to 7, all the *Ansätze* accurately reproduced the positions of peaks for $\omega \lesssim 6$. In general, an insulating system has fewer spectral peaks than metallic cases, allowing the moment expansion by the recursive approach to reproduce the peak positions more accurately. Still, there is some variation among the *Ansätze*, likely due to the fitting error, especially around the small peak near $\omega = 4$. The spectral function shows a tiny peak near $\omega = 0$ as shown in the inset of Fig. 4(b). This is due to the $k = 3$ bath site nearly decoupled from the impurity being physically irrelevant.

Here, we aim to quantify the difference between the spectral functions reconstructed from the exact moments and those calculated via the recursive approach. To this end, we utilize

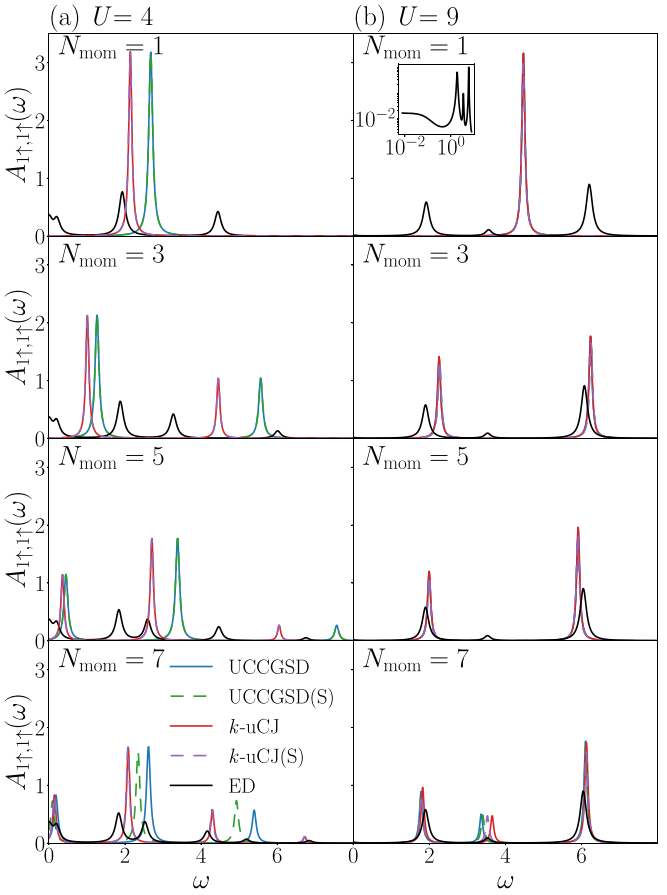

FIG. 4. Computed $A_{1\uparrow,1\uparrow}(\omega)$ for each maximum order $N_{\rm mom}$. (a) and (b) Results for $U = 4$ and $U = 9$, respectively. In the k-uCJ and the k-uCJ(S), we set $k = 5$. ED refers to the spectral functions constructed from exact moments using exact diagonalization. The spectrum of $V = 0.1$ around $\omega = 0$ has a tiny magnitude of 10^{-2}, as shown in the inset.

the Wasserstein metric, quantifying a difference between two distributions [73,74]. Figures 5(a) and 5(b) show the computed Wasserstein metric between the spectral functions from the exact moments at $N_{\rm mom} = 7$ and those using *Ansätze* at each maximum order $N_{\rm mom}$ for $U = 4$ and $U = 9$, respectively. As the maximum order $N_{\rm mom}$ increases, the distance between the two distributions decreases, consistent with the enhanced reproducibility of the spectrum at large $N_{\rm mom}$.

3. Imaginary-time Green's functions

Figures 6(a) and 6(b) show the imaginary-time Green's functions computed from the reconstructed spectral function by the moment expansion for $U = 4$ and $U = 9$, respectively. We use the reconstructed spectral function from the exact moments for each $N_{\rm mom}$ as a reference. In the k-uCJ, we set $k = 5$. In computing the reference data, we filtered out peaks below $\omega \leqslant 10^{-2}$ that are physically irrelevant.

In Fig. 6, for both $U = 4$ and $U = 9$, the differences among the *Ansätze* become less pronounced in the imaginary-time Green's functions compared to the differences in the spectral function. In Fig. 6(a), for $U = 4$, imaginary-time Green's functions exhibit a power-law decay. This necessitates a higher $N_{\rm mom}$ in the moment expansion. However, for

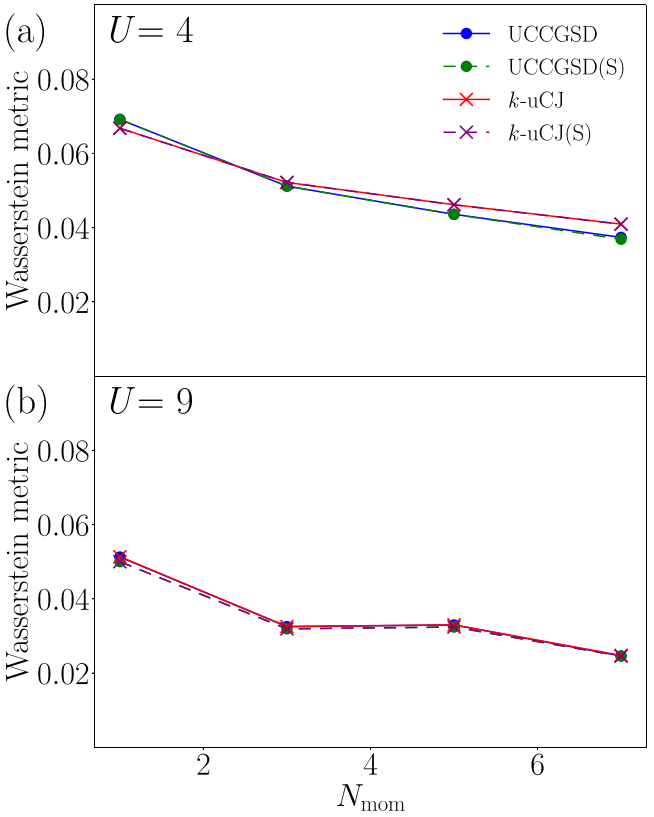

FIG. 5. Computed Wasserstein metric for each maximum order $N_{\rm mom}$. (a and b) Results for $U = 4$ and 9, respectively. In the k-uCJ and the k-uCJ(S), we set $k = 5$.

$\tau > 5$, we observed that increasing $N_{\rm mom}$ did not improve the accuracy due to the exponential growth in the fitting error with $N_{\rm mom}$ in the recursive approach. Only the UCCGSD(S) result seems to diverge from the rest. Nonetheless, its deviation starting at $\tau = 5$ aligns with the trends observed in other *Ansätze*, displaying a comparable pattern. In Fig. 6(b), for $U = 9$, imaginary-time Green's functions exhibit an exponential decay. The Green's functions computed by the recursive approach, even at $N_{\rm mom} = 5$, match the reference data, suggesting a smaller $N_{\rm mom}$ achieves convergence compared to the metallic case.

C. Two-site impurity model

We consider the two-site impurity model with particle-hole symmetry and $N_{\rm bath} = 6$, shown in Fig. 2(b). The number of qubits in this model is 16. The Hamiltonian is given by

$$\begin{aligned}\mathcal{H} = U \sum_{i=1}^{2} \hat{d}^\dagger_{i\uparrow}\hat{d}_{i\uparrow}\hat{d}^\dagger_{i\downarrow}\hat{d}_{i\downarrow} - \mu \sum_{i=1,2}\sum_{\sigma=\uparrow,\downarrow} \hat{d}^\dagger_{i\sigma}\hat{d}_{i\sigma} \\ - t \sum_{\sigma=\uparrow,\downarrow} (\hat{d}^\dagger_{1\sigma}\hat{d}_{2\sigma} + \hat{d}^\dagger_{2\sigma}\hat{d}_{1\sigma}) \\ - \sum_{j=1}^{2}\sum_{k_1=1}^{3}\sum_{k_2=4}^{6}\sum_{\sigma=\uparrow,\downarrow} V(\hat{d}^\dagger_{j\sigma}\hat{c}_{k_j\sigma} + \hat{c}^\dagger_{k_j\sigma}\hat{d}_{j\sigma}) \\ + \sum_{k=1}^{6}\sum_{\sigma=\uparrow,\downarrow} \epsilon_k \hat{c}^\dagger_{k\sigma}\hat{c}_{k\sigma}, \end{aligned} \tag{35}$$

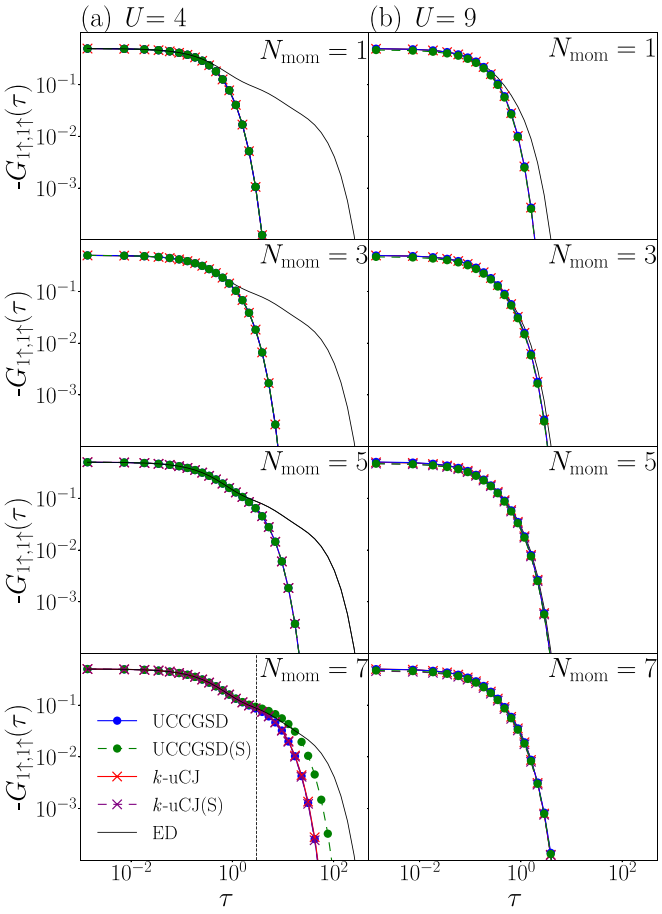

FIG. 6. Computed $G_{1\uparrow,1\uparrow}(\tau)$ for each maximum order $N_{\rm mom}$. (a and b) Results for $U = 4$ and $U = 9$, respectively. In the k-uCJ and the k-uCJ(S), we set $k = 5$. ED refers to the spectral functions constructed from exact moments using exact diagonalization. The black vertical lines in (a) for the maximum order $N_{\rm mom} = 7$ show where the deviation of the reconstructed spectral functions from the reference data starts.

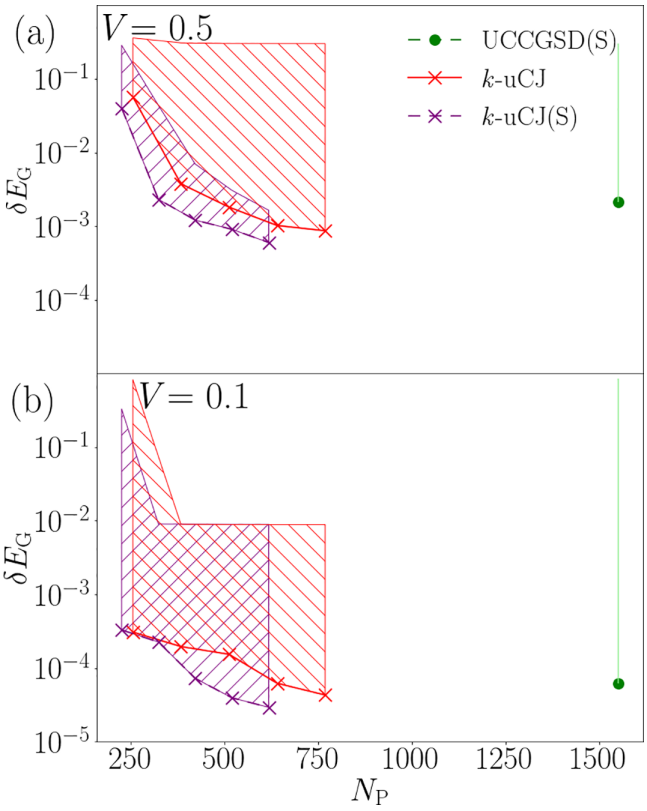

FIG. 7. Computed $\delta E_{\rm G}$ for the two-site impurity model, where the x axis represents the number of parameters $N_{\rm P}$. (a and b) Results for $U = 4$ and $U = 9$, respectively. In the k-uCJ and the k-uCJ(S), k increases from 1 to 5. The markers represent the smallest errors when the initial parameters are changed 20 times. The hatched lines in the figures show how absolute errors depend on initial parameters for k-uCJ and k-uCJ(S), respectively. The vertical lines indicate this dependency for UCCGSD and UCCGSD(S), respectively.

where t represents the hopping between the two impurities. For $V = 0.5$ and $V = 0.1$, we use common bath parameters: $U = 4$, $\mu = U/2$, $t = 1$, and $\epsilon_k = \{1, 0, -1, 1, 0, -1\}$. The case of $V = 0.5$ is expected to be more *metallic* than $V = 0.1$.

1. Ground-state calculation

Figures 7(a) and 7(b) show $\delta E_{\rm G}$ for $V = 0.5$ and $V = 0.1$, respectively. For the k-uCJ and the k-uCJ(S), k was varied from 1 to 5 to check convergence. We omitted the VQE calculation with the UCCGSD because of its prohibitively large number of variational parameters. As before, the markers represent the optimal results obtained from 20 variations of the initial variational parameters for each *ansatz*. The hatched lines highlight the dependency of each *ansatz* on initial guesses.

In the three *Ansätze*, the ground-state energies are reproduced with comparable accuracy. Considering $N_{\rm P}$, both k-uCJ and k-uCJ(S) are more efficient than UCCGSD(S). The results for the sparse *Ansätze* in Figs. 7(a) and 7(b) show that we can reduce the number of the variational parameters associated with bath sites without sacrificing ground-state accuracy in the cluster impurity model. The sparse *Ansätze* are also applicable for the case of $V = 0.5$, which exhibits more metallic characteristics. For the k-uCJ, $N_{\rm P}$ is reduced from [256, 384, 512, 640, 768] to [226, 324, 422, 520, 618] for $k = 1, 2, \ldots, 5$.

2. Spectral functions

Figures 8(a) and 8(b) show the reconstructed spectral functions using the moment expansion for $V = 0.5$ and $V = 0.1$, respectively. We computed the reference data from the exact moments for each $N_{\rm mom}$ using exact diagonalization. In the k-uCJ, we set $k = 5$. We omitted the moment calculations using UCCGSD for the same reasons as the ground-state calculations.

In Fig. 8(a), for $V = 0.5$, increasing $N_{\rm mom}$ tends to enhance the representation of several spectral peaks. Yet, it remains challenging to comprehensively capture the entire structure, mainly due to the fitting error observing no improvement beyond $N_{\rm mom} = 7$. In Fig. 8(b), for $V = 0.1$, by increasing the maximum order $N_{\rm mom}$ up to 5, all the *Ansätze* accurately reproduced the positions of several peaks for $\omega \lesssim 4$. This indicates that an insulating system with fewer spectral peaks offers the advantage of accurately determining peak positions. However, variations around the small peak near $\omega = 1$ among

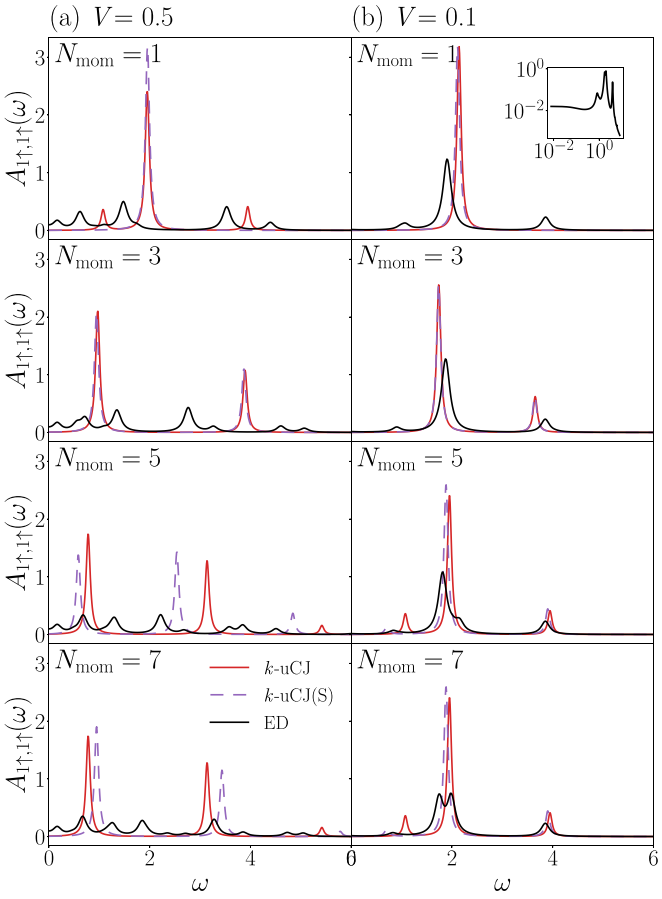

FIG. 8. Computed $A_{1\uparrow,1\uparrow}(\omega)$ for each maximum order N_{mom}. (a and b) Results for $V = 0.5$ and $V = 0.1$, respectively. In the k-uCJ and the k-uCJ(S), we set $k = 5$. ED refers to the spectral functions constructed from exact moments using exact diagonalization. The spectrum for $V = 0.1$ has a tiny peak around $\omega = 0$, as shown in the inset.

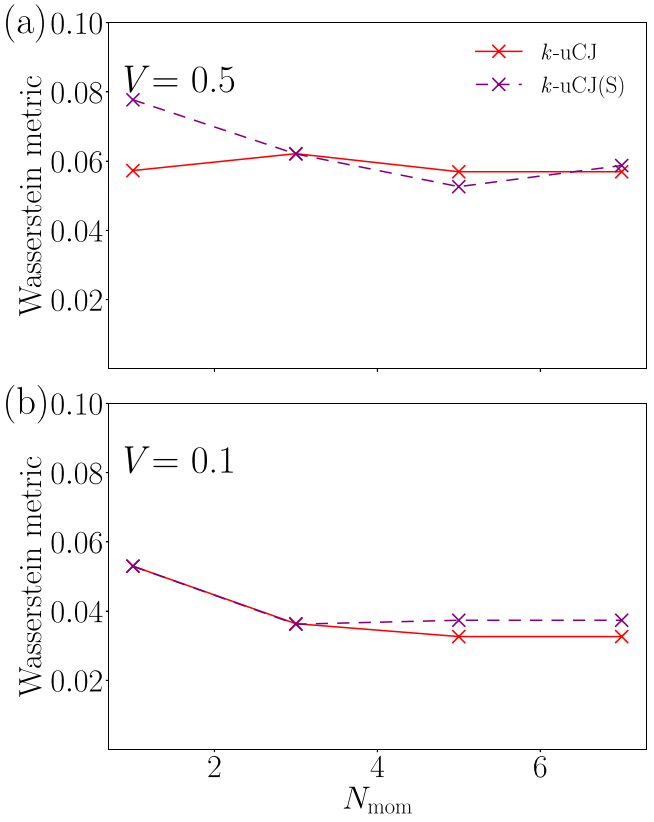

FIG. 9. Computed Wasserstein metric between the spectral functions constructed from exact moments and those computed using the *Ansätze* for the two-site impurity model for each maximum order N_{mom}. (a and b) Results for $V = 0.5$ and 0.1, respectively. In the k-uCJ and the k-uCJ(S), we set $k = 5$.

the *Ansätze* likely result from the fitting error. The spectral function shows a small peak around $\omega = 0$ as shown in Fig. 8(b). This originates from bath sites weakly coupled with the impurity being physically insignificant.

Figures 9(a) and 9(b) show the computed Wasserstein metrics between the spectral functions reconstructed from the exact moments at $N_{\mathrm{mom}} = 7$ and those computed using the *Ansätze* at each maximum order N_{mom} for $V = 0.5$ and $V = 0.1$, respectively. Due to the influence of noise, the distances, especially for $N_{\mathrm{mom}} \geqq 5$, stay at higher values than those without shot noise. Still, the Wasserstein metric tends to decrease as the maximum order N_{mom} increases, which is consistent with the improved reproducibility of the spectral functions reconstructed by the moment expansion.

3. Imaginary-time Green's functions

Figures 10(a) and 10(b) show the imaginary-time Green's functions computed from the moment expansion for $V = 0.5$ and $V = 0.1$, respectively, with the k-uCJ *ansatz* with $k = 5$. We computed the reference data from the reconstructed spectral function using exact moments for each N_{mom}. In this computation, we removed the physically irrelevant peaks below $\omega = 10^{-2}$ in the spectrum (see the inset of Fig. 8). In Fig. 10, for both $V = 0.5$ and $V = 0.1$, the differences among the *Ansätze* become less pronounced in imaginary-time Green's functions compared to the cases of spectral functions. In Fig. 10(a), for $V = 0.5$, the imaginary-time Green's functions exhibit a power-law decay. We observed no improvement by increasing N_{P}, likely due to the fitting error in computing spectral moments. In Fig. 10(b), for $V = 0.1$, imaginary-time Green's functions exhibit an exponential decay. The results with $N_{\mathrm{mom}} = 5$ agree with the reference data.

V. FINITE SHOT SIMULATIONS

In this section, we explore the impact of shot noise for the single-site impurity model with $N_{\mathrm{bath}} = 3$ to evaluate the feasibility of the proposed method on quantum devices. We first optimize variational parameters for the ground state and the intermediate states in the computation of the spectral moments [Eqs. (18) and (23)] using state vector simulations as detailed in Sec. IV. Then, we measure the expectation values of the Hamiltonian and the transition amplitude (25) for each order of the moment m with a finite number of measurements. It should be noted that the effect of the shot noise was not considered during the optimization steps. This noise affects the measured scalar values, the ground-state energy

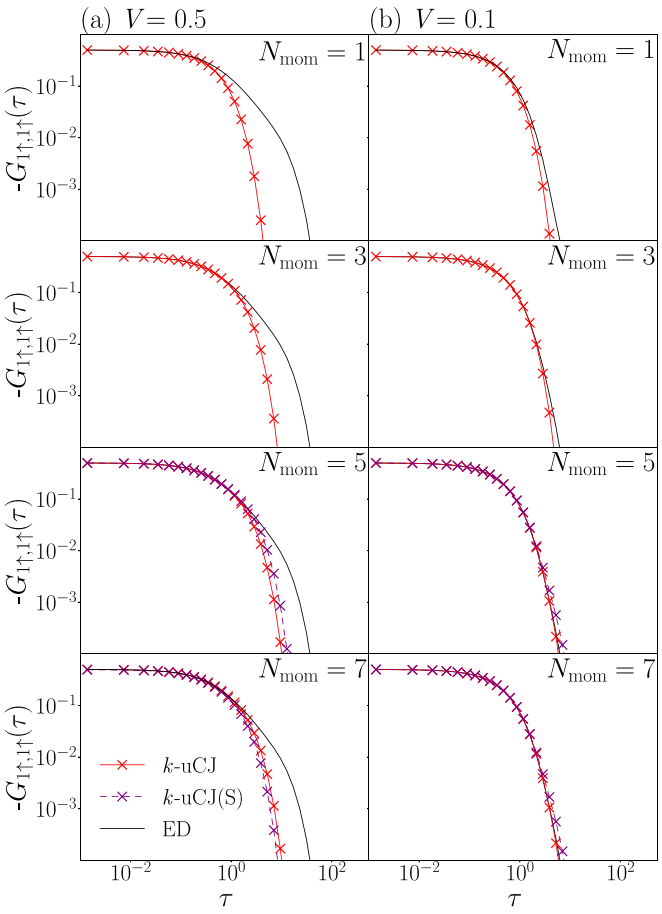

FIG. 10. Computed $G_{1\uparrow,1\uparrow}(\tau)$ for each maximum order N_{mom}. (a and b) Results for $V = 0.5$ and $V = 0.1$, respectively. In the k-uCJ and the k-uCJ(S), we set $k = 5$. ED refers to the spectral functions constructed from exact moments computed by exact diagonalization. The black vertical lines in (a) for $N_{\mathrm{mom}} = 7$ show where the deviation of the reconstructed spectral functions from the reference data starts.

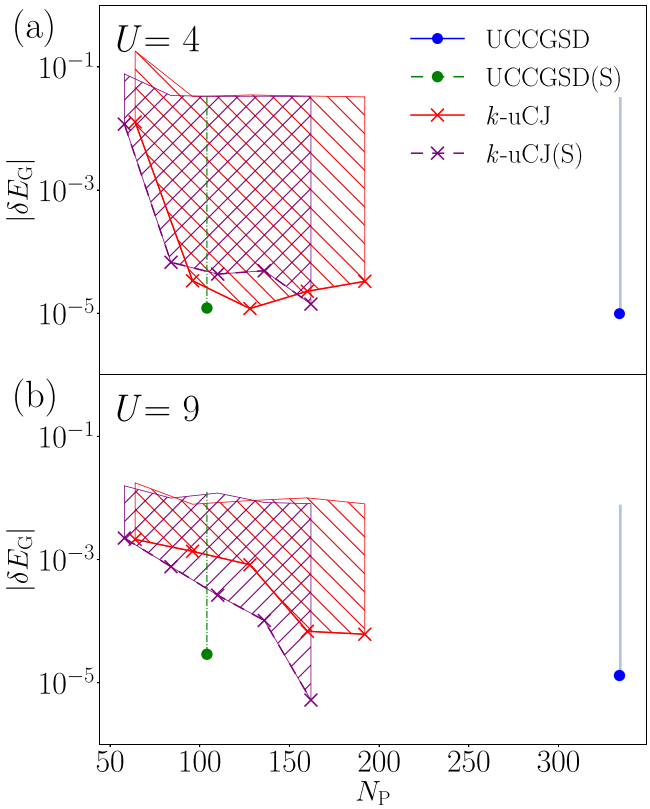

FIG. 11. Computed δE_{G} with 30 000 measurements for the single-site impurity model, where the x axis represents the number of parameters N_{P}. (a and b) Results for $U = 4$ and $U = 9$, respectively. In the k-uCJ and the k-uCJ(S), k was varied from 1 to 5. The markers represent the best result obtained by varying the initial parameters 50 times. The hatched lines in the figures show how absolute errors depend on initial parameters for k-uCJ and k-uCJ(S), while the vertical lines indicate this dependency for UCCGSD and UCCGSD(S).

E_{G} and coefficients $d_0, d_1, \ldots, d_{\mathrm{mom}}$ in the recursive approach [Eq. (25)]. We set the number of measurements to 30 000.

A. Ground-state calculation

Figures 11(a) and 11(b) show δE_{G} computed with shot noise for $U = 4$ and $U = 9$, respectively. The markers represent the best results obtained by varying the initial parameters 50 times for each *ansatz*. As indicated by the shaded area, the issue of initial parameter dependency remains significant in the presence of shot noise.

In all four *Ansätze*, statistical errors with a finite number of measurements reduce the overall accuracy compared to the results without shot noise (see Fig. 3). Still, the ground-state energies can be reproduced with comparative accuracy among *Ansätze*. The results for the sparse *Ansätze* in Figs. 11(a) and 11(b) show that reducing the variational parameters associated with bath sites does not compromise the accuracy of E_{G}. The accuracy of the k-uCJ(S) is lower than that of the k-uCJ for the *metallic* system ($U = 4$), which may be attributed to statistical error.

B. Spectral functions

Figures 12(a) and 12(b) show the reconstructed spectral functions using the spectral moment computed with shot noise for $U = 4$ and $U = 9$, respectively. We set $k = 5$ in the k-uCJ. In Fig. 12(a), for $U = 4$, none of the *Ansätze* reconstruct the spectral peaks. These discrepancies primarily stem from numerical errors in the moment calculations. It should be noted that reconstructing a spectral function from the moments is not a well-conditioned problem (although more robust than traditional numerical analytic continuation from imaginary time due to the analytic procedure). Specifically, in the shot noise simulation, such errors are attributed to statistical error, the limited representational capability of the *Ansätze*, and optimization issues. The effect of statistical noise is dominant when comparing the calculation results to the case without shot noise Fig. 4. In Fig. 12(b), for $U = 9$, the shot noise induces small shifts in the positions of several peaks for $\omega \lesssim 6$ compared to the results computed without the shot noise. There are some variations among the *Ansätze*, likely due to the fitting error, but generally, the agreement is much improved compared to the more metallic $U = 4$ results.

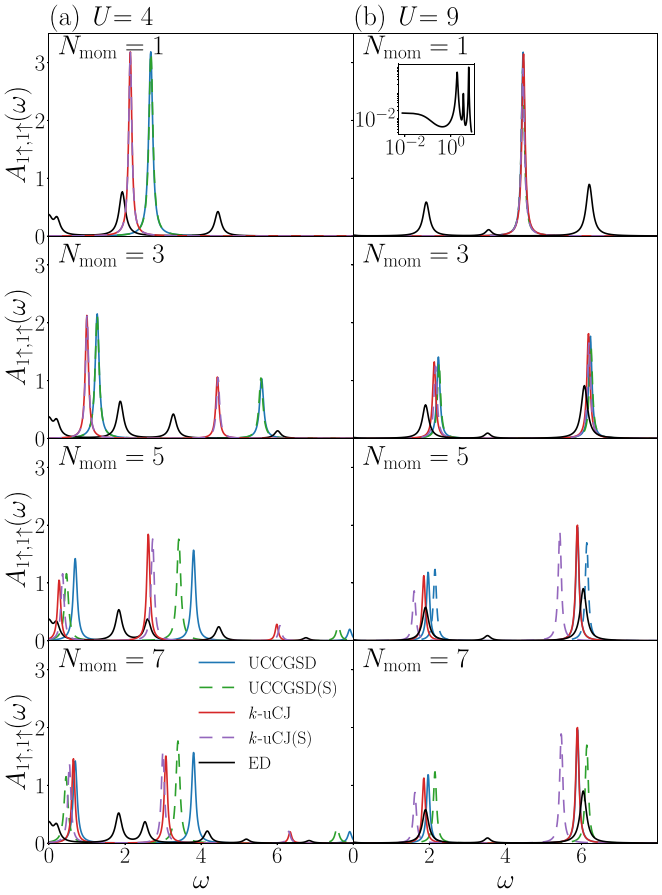

FIG. 12. Computed $A_{1\uparrow,1\uparrow}(\omega)$ with 30 000 measurements for each maximum order N_{mom}. In the k-uCJ and the k-uCJ(S), we set $k = 5$. ED refers to the spectral functions constructed from exact moments using exact diagonalization. (a and b) Results for $U = 4$ and $U = 9$, respectively.

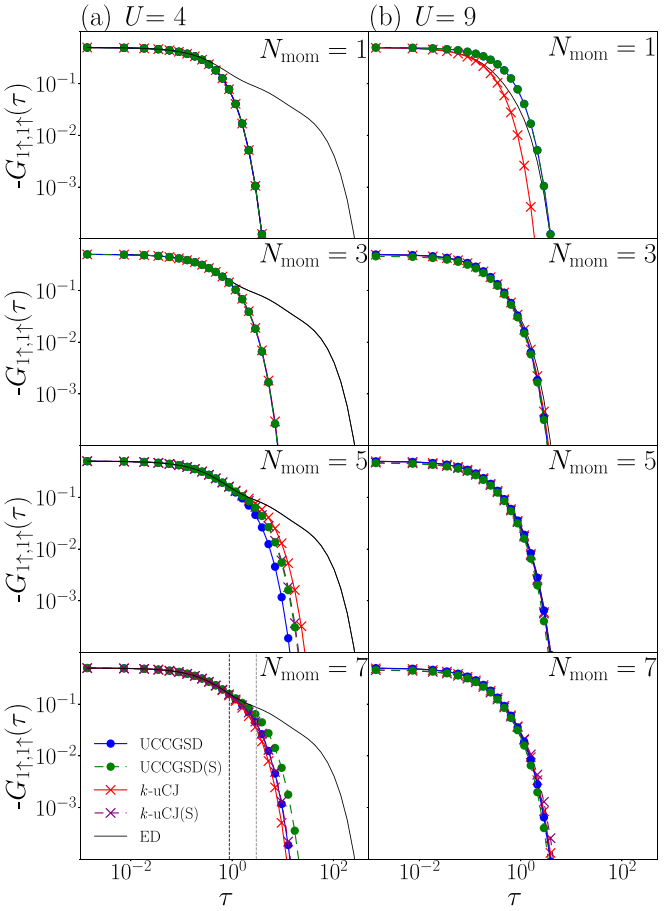

FIG. 13. Computed $G_{1\uparrow,1\uparrow}(\tau)$ with 30 000 measurements for each maximum order N_{mom}. (a and b) Results for $U = 4$ and $U = 9$, respectively. In the k-uCJ and the k-uCJ(S), we set $k = 5$. ED refers to the spectral functions constructed from exact moments using exact diagonalization. The black vertical lines in (a) for $N_{\mathrm{mom}} = 7$ indicate where the reconstructed spectral functions with shot noise begin to differ from those derived from exact moments. The gray line indicates the case without shot noise (see Fig. 6).

C. Imaginary-time Green's functions

We now compute the imaginary-time Green's functions from the reconstructed spectral functions by the moment expansion with the shot noise. Figures 13(a) and 13(b) show the results for $U = 4$ and 9, respectively. In the k-uCJ, we set $k = 5$.

For both $U = 4$ and $U = 9$, despite the large deviations in the spectral functions due to the fitting error, these variations are suppressed in the reconstructed imaginary-time Green's functions. The results from all the *Ansätze* are consistent up to $\tau \approx 1$, then they start to deviate. This is because the imaginary-time Green's function is insensitive to changes in the associated spectral function. In Fig. 13(a), for $U = 4$ with $N_{\mathrm{mom}} = 7$, due to the shot noise, the black vertical line at $\tau = 1$ marks the earlier start of deviation, while the gray vertical line at $\tau = 5$ indicates the start without shot noise (see Fig. 6). In Fig. 13(b), for $U = 4$ with $N_{\mathrm{mom}} = 5$, the results with shot noise are in good agreement with the reference data. These results indicate the moment expansion can successfully calculate the imaginary-time Green's functions under the influence of shot noise. The imaginary-time Green's function, as calculated in this way, is sufficient for performing self-consistent calculations of DMFT. After convergence, some quantities computed from the imaginary-time Green's function (e.g., electron occupancy) are expected to be less sensitive to noise than real-frequency spectral functions.

VI. SUMMARY AND DISCUSSION

In this paper, we proposed compact quantum circuits for quantum impurity models with a star-like bath geometry by sparsifying the UCCGSD and k-uCJ *ansatz*. These forms have a significant parameter scaling of N_{SO}^4 and N_{SO}^2, respectively, which are reduced by removing insignificant variational parameters associated with two-body coupling between bath sites. This results in a reduced number of variational parameters scaling as $O(N_{\mathrm{imp}}^4)$ and $O(N_{\mathrm{imp}}^2)$ for the UCCGSD(S) and k-uCJ(S) *ansatz*, respectively. We numerically demonstrated that the compact *Ansätze* can accurately reproduce the ground-state energies for typical quantum impurity models, with and without shot noise. In the moment calculations for

dynamic quantities, to avoid measuring more Pauli-operator terms at higher orders, we proposed a recursive method similar to VQE. We also demonstrated that, when combined with the suggested *Ansätze*, the moment expansion effectively computes the imaginary-time Green's function, even in the presence of shot noise.

Before concluding this paper, we compare the proposed *Ansätze* and the spectral moments with other approaches. Previous studies utilized an adaptive variational quantum eigensolver (ADAPT-VQE) for impurity models [34,75]. While ADAPT-VQE can provide near-exact solutions with a deep circuit, it demands more measurements for gradient computation than traditional VQE. Also, its success depends on the selected operator pool, which makes it hard to compare it to other approaches. In addition, it is instructive to compare the moment expansion to alternative approaches such as the VQS approach [36], with which the method bears many similarities. The moment expansion preserves the causal nature of the spectral functions; however, it encounters growing fitting errors in the recursive approach, most significantly in metallic systems. The VQS method might handle these systems more effectively via time evolution over a longer time span. Still, it could be costly since it requires computing all variational parameters at every time step. A more detailed comparison is left for future studies.

Finally, we discuss the potential future research directions. Firstly, it should be noted that the noise is underestimated because the effect of shot noise has not been taken into account in the optimization steps. To ensure the accuracy of energy and spectral moments, a substantial number of measurements are required for gradient calculations during optimization. This requirement challenges current quantum computers. In addressing this issue, when optimizing in the VQE, employing robust optimization methods against noise [76,77] as well as noise mitigation techniques is crucial [78,79]. Secondly, the initial parameter selection plays a crucial role in the accuracy of ground-state energies and moments. Specifically, the accuracy of the moment is closely tied to that of the ground state. The selection of optimal initial parameters to avoid local minima and metastable solutions should be a critical area of future studies. Thirdly, minimizing the number of measurements in VQE and the recursive approach is essential in the context of utilizing near-term quantum devices. One viable solution is the efficient grouping of observables for simultaneous measurement [80]. Fourthly, it is also important to investigate how the noise in the measured Green's function and discretization errors of the bath propagate during self-consistent calculations in DMFT and affect quantities of interest, e.g., momentum-resolved spectrum. Developing methods for suppressing such errors is crucial. Fifthly, the potential applicability of sparse *Ansätze* to other impurity models with star-like geometry, such as multiorbital systems, requires further investigation. There might be a possibility that sparse *Ansätze* are a reasonable approach for models other than impurity models. Specifically, in molecular models that feature tree-like structures [81], applying a sparse *ansatz* could potentially be a plausible approach. Lastly, incorporating the concept of sparsity into classical variational algorithmic approaches, such as machine learning wave functions [82,83], may improve computational efficiency.

ACKNOWLEDGMENTS

H.S. was supported by JSPS KAKENHI Grants No. 18H01158, No. 21H01041, No. 21H01003, and No. 23H03817, Japan. R.S. and H.S. were supported by JST PRESTO Grant No. JPMJPR2012, Japan. W.M. was supported by funding from the MEXT Quantum Leap Flagship Program (MEXTQLEAP) through Grant No. JPMXS0120319794, and the JST COI-NEXT Program through Grant No. JPMJPF2014. W.M. also acknowledges support from JSPS KAKENHI Grants No. JP23H03819 and No. JP21K18933. G.H.B. and O.J.B. were supported by funding from European Union's Horizon 2020 research and innovation programme under Grant Agreement No. 759063, as well as EPSRC Grants No. EP/Y005244/1 (VSL-Q) and No. EP/W032635/1 (RoaRQ). We thank the Supercomputer Center, the Institute for Solid State Physics, the University of Tokyo for the use of the facilities.

APPENDIX A: A QUANTUM CIRCUIT TO COMPUTE TRANSITION AMPLITUDE

We evaluate the transition amplitude on a quantum computer by measuring the Hermitian and anti-Hermitian parts of the following form:

$$\langle 0|U_1^\dagger P U_2|0\rangle, \tag{A1}$$

where P are Pauli operators with m qubits, and U_1 and U_2 are unitary operators with m qubits. Equation (A1) can be measured using the quantum circuit in Fig. 14 [49,50,84], which requires one ancilla qubit.

Let p_0/p_1 be the probability of measuring $0/1$ in the ancilla qubit. The real and imaginary parts of the transition amplitude can be measured separately by setting $\phi = 0$ and $\pi/2$ in the R_z gate, respectively, as

$$p_0 - p_1 = \begin{cases} \mathrm{Re}\langle 0|U_1^\dagger(\vec{\theta}_1) P U_2(\boldsymbol{\theta}_2)|0\rangle & \phi = 0, \\ -\mathrm{Im}\langle 0|U_1^\dagger(\vec{\theta}_1) P U_2(\boldsymbol{\theta}_2)|0\rangle & \phi = \pi/2. \end{cases} \tag{A2}$$

As this method is based on a single ancilla qubit, we need complex quantum circuits for NISQ devices because of the control unitary operators.

APPENDIX B: MOMENT CALCULATIONS VIA THE RECURSIVE VQE

This Appendix shows the computed spectral moments via VQE and recursive VQE for the single-site impurity model with $N_{\mathrm{imp}} = 3$, with or without shot noise.

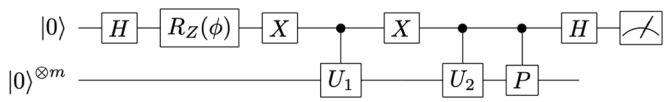

FIG. 14. Quantum circuit for computing the transition amplitude in Eq. (A1). The quantum circuit employs m qubits (on the bottom line) and one additional qubit as an ancilla (on the top line). The transition amplitude can be obtained by summing the measurement outcomes of the ancilla qubit for the Z basis.

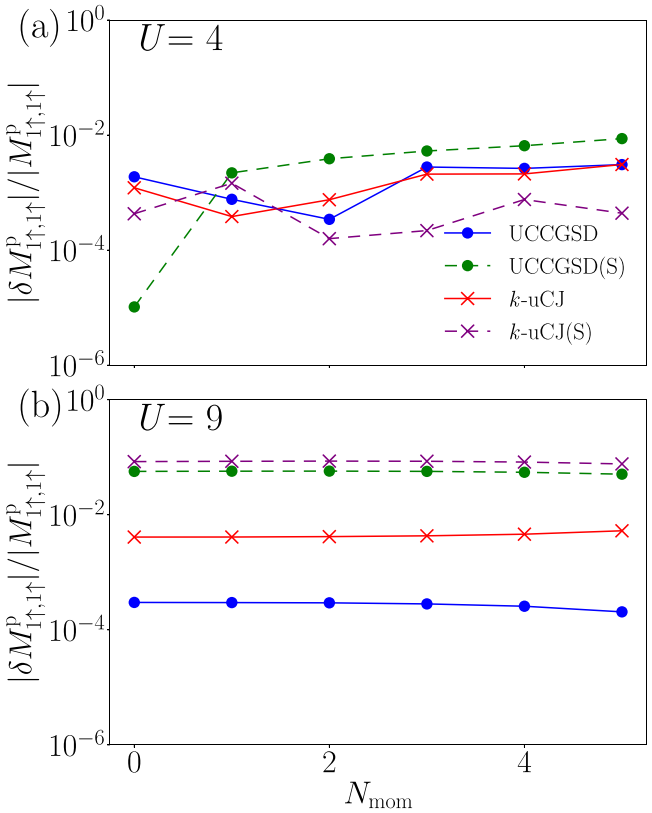

FIG. 15. Computed $|\delta M^{\mathrm{p}}_{rs}|/M^{\mathrm{p}}_{rs}$ for the single-site impurity model. (a and b) Results for $U = 4$ and $U = 9$, respectively. In the k-uCJ and the k-uCJ(S), we set $k = 5$.

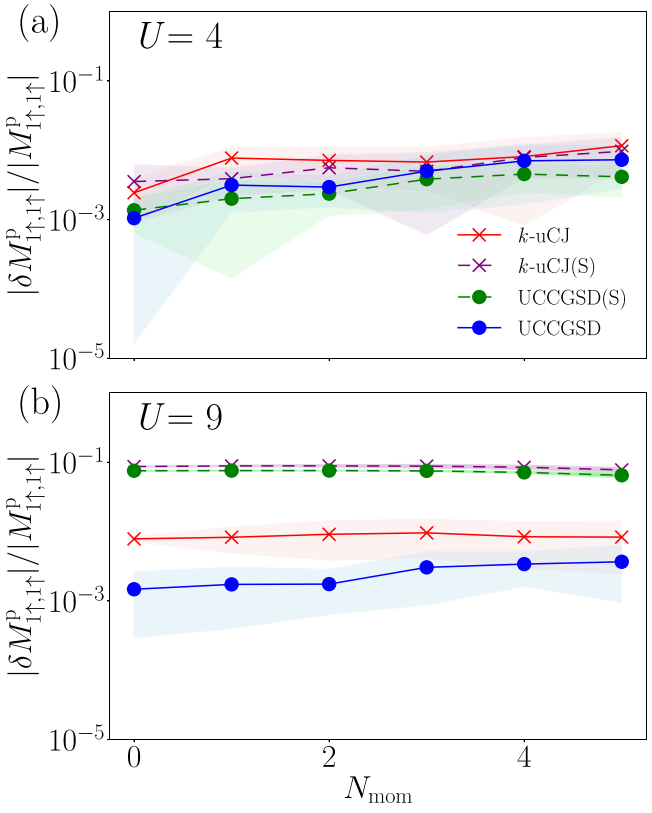

FIG. 16. Computed $|\delta M^{\mathrm{p}}_{rs}|/M^{\mathrm{p}}_{rs}$ for the single-site impurity model with shot noise. (a and b) Results for $U = 4$ and $U = 9$, respectively. In the k-uCJ and the k-uCJ(S), we set $k = 5$. The markers indicate the mean, while the lightly shaded areas represent the standard deviation.

1. State vector simulation

Figures 15(a) and 15(b) show the relative error of the spectral moments $|\delta M^{\mathrm{p}}_{rs}|/|M^{\mathrm{p}}_{rs}|$ for $U = 4$ and $U = 9$, respectively. $|\delta M^{\mathrm{p}}_{rs}|/|M^{\mathrm{p}}_{rs}|$ are calculated via VQE or recursive VQE and exact diagonalization. The relative error for each *ansatz* remains nearly constant. In Fig. 15(a), for $U = 4$, the k-uCJ(S) has the highest accuracy at $N_{\mathrm{mom}} = 5$, followed by the k-uCJ, UCCGSD. In Fig. 15(b), for $U = 9$, the UCCGSD has the highest accuracy, followed by the k-uCJ.

2. Shot noise

Figures 16(a) and 16(b) show the relative errors of the spectral moments $|\delta M^{\mathrm{p}}_{rs}|/|M^{\mathrm{p}}_{rs}|$ with a finite number of measurements, 30 000 for $U = 4$ and $U = 9$, respectively. The markers in the figure denote the mean, and the lightly shaded areas indicate the standard deviation derived from the calculation repeated ten times with shot noise for each *ansatz*. The sparse *ansatz* is generally less accurate than the original *ansatz* due to the shot noise. In Fig. 15(a), for $U = 4$, no significant difference in relative error between *Ansätze* was observed due to the shot noise. Still, the relative error for each *ansatz* remains nearly constant.

[1] A. J. Leggett, What DO we know about high T_c? Nat. Phys. **2**, 134 (2006).

[2] B. Keimer, S. A. Kivelson, M. R. Norman, S. Uchida, and J. Zaanen, From quantum matter to high-temperature superconductivity in copper oxides, Nature (London) **518**, 179 (2015).

[3] A. Georges, G. Kotliar, W. Krauth, and M. J. Rozenberg, Dynamical mean-field theory of strongly correlated fermion systems and the limit of infinite dimensions, Rev. Mod. Phys. **68**, 13 (1996).

[4] G. Kotliar, S. Y. Savrasov, K. Haule, V. S. Oudovenko, O. Parcollet, and C. A. Marianetti, Electronic structure calculations with dynamical mean-field theory, Rev. Mod. Phys. **78**, 865 (2006).

[5] G. Knizia and G. K.-L. Chan, Density matrix embedding: A simple alternative to dynamical mean-field theory, Phys. Rev. Lett. **109**, 186404 (2012).

[6] C. J. C. Scott and G. H. Booth, Extending density matrix embedding: A static two-particle theory, Phys. Rev. B **104**, 245114 (2021).

[7] N.-O. Linden, M. Zingl, C. Hubig, O. Parcollet, and U. Schollwöck, Imaginary-time matrix product state impurity solver in a real material calculation: Spin-orbit

coupling in Sr_2RuO_4, Phys. Rev. B **101**, 041101(R) (2020).
[8] F. A. Wolf, A. Go, I. P. McCulloch, A. J. Millis, and U. Schollwöck, Imaginary-time matrix product state impurity solver for dynamical mean-field theory, Phys. Rev. X **5**, 041032 (2015).
[9] D. Bauernfeind, M. Zingl, R. Triebl, M. Aichhorn, and H. G. Evertz, Fork tensor-product states: Efficient multiorbital real-time DMFT solver, Phys. Rev. X **7**, 031013 (2017).
[10] E. Gull, A. J. Millis, A. I. Lichtenstein, A. N. Rubtsov, M. Troyer, and P. Werner, Continuous-time Monte Carlo methods for quantum impurity models, Rev. Mod. Phys. **83**, 349 (2011).
[11] A. Y. Kitaev, Quantum measurements and the Abelian stabilizer problem, arXiv:quant-ph/9511026 [quant-ph].
[12] A. Aspuru-Guzik, A. D. Dutoi, P. J. Love, and M. Head-Gordon, Simulated quantum computation of molecular energies, Science **309**, 1704 (2005).
[13] E. Farhi, J. Goldstone, S. Gutmann, and M. Sipser, Quantum computation by adiabatic evolution arXiv:quant-ph/0001106 [quant-ph].
[14] T. Albash and D. A. Lidar, Adiabatic quantum computation, Rev. Mod. Phys. **90**, 015002 (2018).
[15] B. Bauer, D. Wecker, A. J. Millis, M. B. Hastings, and M. Troyer, Hybrid quantum-classical approach to correlated materials, Phys. Rev. X **6**, 031045 (2016).
[16] A. Peruzzo, J. McClean, P. Shadbolt, M.-H. Yung, X.-Q. Zhou, P. J. Love, A. Aspuru-Guzik, and J. L. O'brien, A variational eigenvalue solver on a photonic quantum processor, Nat. Commun. **5**, 4213 (2014).
[17] S. McArdle, T. Jones, S. Endo, Y. Li, S. C. Benjamin, and X. Yuan, Variational ansatz-based quantum simulation of imaginary time evolution, npj Quantum Inf. **5**, 75 (2019).
[18] J. Preskill, Quantum computing in the NISQ era and beyond, Quantum **2**, 79 (2018).
[19] P. Besserve and T. Ayral, Unraveling correlated material properties with noisy quantum computers: Natural orbitalized variational quantum eigensolving of extended impurity models within a Slave-Boson approach, Phys. Rev. B **105**, 115108 (2022).
[20] S. Backes, Y. Murakami, S. Sakai, and R. Arita, Dynamical mean-field theory for the Hubbard-Holstein model on a quantum device, Phys. Rev. B **107**, 165155 (2023).
[21] I. Rungger, N. Fitzpatrick, H. Chen, C. H. Alderete, H. Apel, A. Cowtan, A. Patterson, D. M. Ramo, Y. Zhu, N. H. Nguyen, E. Grant, S. Chretien, L. Wossnig, N. M. Linke, and R. Duncan, Dynamical mean field theory algorithm and experiment on quantum computers, arXiv:1910.04735 [quant-ph].
[22] G. Greene-Diniz, D. Z. Manrique, K. Yamamoto, E. Plekhanov, N. Fitzpatrick, M. Krompiec, R. Sakuma, and D. M. Ramo, Quantum computed Green's functions using a cumulant expansion of the Lanczos method, arXiv:2309.09685 [cond-mat.str-el].
[23] D. Dhawan, D. Zgid, and M. Motta, Quantum algorithm for imaginary-time Green's functions, arXiv:2309.09914 [quant-ph].
[24] B. Jaderberg, A. Agarwal, K. Leonhardt, M. Kiffner, and D. Jaksch, Minimum hardware requirements for hybrid quantum-classical DMFT, Quantum Sci. Technol. **5**, 034015 (2020).
[25] S. Bravyi and D. Gosset, Complexity of quantum impurity problems, Commun. Math. Phys. **356**, 451 (2017).
[26] M. Nusspickel and G. H. Booth, Efficient compression of the environment of an open quantum system, Phys. Rev. B **102**, 165107 (2020).
[27] H. Shinaoka and Y. Nagai, Sparse modeling of large-scale quantum impurity models with low symmetries, Phys. Rev. B **103**, 045120 (2021).
[28] I. de Vega, U. Schollwöck, and F. A. Wolf, How to discretize a quantum bath for real-time evolution, Phys. Rev. B **92**, 155126 (2015).
[29] C. Mejuto-Zaera, L. Zepeda-Núñez, M. Lindsey, N. Tubman, B. Whaley, and L. Lin, Efficient hybridization fitting for dynamical mean-field theory via semi-definite relaxation, Phys. Rev. B **101**, 035143 (2020).
[30] R. J. Bartlett, S. A. Kucharski, and J. Noga, Alternative coupled-cluster *Ansätze* II. The unitary coupled-cluster method, Chem. Phys. Lett. **155**, 133 (1989).
[31] A. G. Taube and R. J. Bartlett, New perspectives on unitary coupled-cluster theory, Int. J. Quantum Chem. **106**, 3393 (2006).
[32] I. Magoulas and F. A. Evangelista, Unitary coupled cluster: Seizing the quantum moment, J. Phys. Chem. A **127**, 6567 (2023).
[33] Y. Yao, F. Zhang, C.-Z. Wang, K.-M. Ho, and P. P. Orth, Gutzwiller hybrid quantum-classical computing approach for correlated materials, Phys. Rev. Res. **3**, 013184 (2021).
[34] A. Mukherjee, N. F. Berthusen, J. C. Getelina, P. P. Orth, and Y.-X. Yao, Comparative study of adaptive variational quantum eigensolvers for multi-orbital impurity models, Commun. Phys. **6**, 4 (2023).
[35] J. Lee, W. J. Huggins, M. Head-Gordon, and K. B. Whaley, Generalized unitary coupled cluster wave functions for quantum computation, J. Chem. Theory Comput. **15**, 311 (2019).
[36] R. Sakurai, W. Mizukami, and H. Shinaoka, Hybrid quantum-classical algorithm for computing imaginary-time correlation functions, Phys. Rev. Res. **4**, 023219 (2022).
[37] X. Yuan, S. Endo, Q. Zhao, Y. Li, and S. C. Benjamin, Theory of variational quantum simulation, Quantum **3**, 191 (2019).
[38] Y. Matsuzawa and Y. Kurashige, Jastrow-type decomposition in quantum chemistry for low-depth quantum circuits, J. Chem. Theory Comput. **16**, 944 (2020).
[39] P. Jordan and E. Wigner, Über das Paulische Äquivalenzverbot, Z. Phys. **47**, 631 (1928).
[40] S. B. Bravyi and A. Y. Kitaev, Fermionic quantum computation, Ann. Phys. **298**, 210 (2002).
[41] J. T. Seeley, M. J. Richard, and P. J. Love, The Bravyi-Kitaev transformation for quantum computation of electronic structure, J. Chem. Phys. **137**, 224109 (2012).
[42] J. Tilly, H. Chen, S. Cao, D. Picozzi, K. Setia, Y. Li, E. Grant, L. Wossnig, I. Rungger, G. H. Booth, and J. Tennyson, The variational quantum eigensolver: A review of methods and best practices, Phys. Rep. **986**, 1 (2022).
[43] P. V. Sriluckshmy, M. Nusspickel, E. Fertitta, and G. H. Booth, Fully algebraic and self-consistent effective dynamics in a static quantum embedding, Phys. Rev. B **103**, 085131 (2021).
[44] O. J. Backhouse and G. H. Booth, Constructing "full-frequency" spectra via moment constraints for coupled cluster Green's functions, J. Chem. Theory Comput. **18**, 6622 (2022).
[45] O. J. Backhouse and G. H. Booth, Dynamics from statics: A conceptual reformulation of Green's, Ph.D. thesis, King's College London, 2023.

[46] H. Weikert, H. Meyer, L. S. Cederbaum, and F. Tarantelli, Block Lanczos and many-body theory: Application to the one-particle Green's function, J. Chem. Phys. **104**, 7122 (1996).
[47] C. J. C. Scott, O. J. Backhouse, and G. H. Booth, A "moment-conserving" reformulation of GW theory, J. Chem. Phys. **158**, 124102 (2023).
[48] O. J. Backhouse, A. Santana-Bonilla, and G. H. Booth, Scalable and predictive spectra of correlated molecules with moment truncated iterated perturbation theory, J. Phys. Chem. Lett. **12**, 7650 (2021).
[49] H. Chen, M. Nusspickel, J. Tilly, and G. H. Booth, Variational quantum eigensolver for dynamic correlation functions, Phys. Rev. A **104**, 032405 (2021).
[50] Y. Ibe, Y. O. Nakagawa, N. Earnest, T. Yamamoto, K. Mitarai, Q. Gao, and T. Kobayashi, Calculating transition amplitudes by variational quantum deflation, Phys. Rev. Res. **4**, 013173 (2022).
[51] T. Jones, S. Endo, S. McArdle, X. Yuan, and S. C. Benjamin, Variational quantum algorithms for discovering Hamiltonian spectra, Phys. Rev. A **99**, 062304 (2019).
[52] O. Higgott, D. Wang, and S. Brierley, Variational quantum computation of excited states, Quantum **3**, 156 (2019).
[53] P. J. Ollitrault, A. Kandala, C.-F. Chen, P. K. Barkoutsos, A. Mezzacapo, M. Pistoia, S. Sheldon, S. Woerner, J. M. Gambetta, and I. Tavernelli, Quantum equation of motion for computing molecular excitation energies on a noisy quantum processor, Phys. Rev. Res. **2**, 043140 (2020).
[54] F. Zhang, N. Gomes, Y. Yao, P. P. Orth, and T. Iadecola, Adaptive variational quantum eigensolvers for highly excited states, Phys. Rev. B **104**, 075159 (2021).
[55] M. Nooijen, Can the eigenstates of a many-body Hamiltonian be represented exactly using a general two-body cluster expansion? Phys. Rev. Lett. **84**, 2108 (2000).
[56] W. Kutzelnigg, Quantum chemistry in Fock space. I. The universal wave and energy operators, J. Chem. Phys. **77**, 3081 (1982).
[57] W. Kutzelnigg and S. Koch, Quantum chemistry in Fock space. II. Effective Hamiltonians in Fock space, J. Chem. Phys. **79**, 4315 (1983).
[58] W. Kutzelnigg, Quantum chemistry in Fock space. IV. The treatment of permutational symmetry. Spin-free diagrams with symmetrized vertices, J. Chem. Phys. **82**, 4166 (1985).
[59] W. Kutzelnigg, Error analysis and improvements of coupled-cluster theory, Theoret. Chim. Acta **80**, 349 (1991).
[60] P. J. J. O'Malley *et al.*, Scalable quantum simulation of molecular energies, Phys. Rev. X **6**, 031007 (2016).
[61] P. K. Barkoutsos, J. F. Gonthier, I. Sokolov, N. Moll, G. Salis, A. Fuhrer, M. Ganzhorn, D. J. Egger, M. Troyer, A. Mezzacapo *et al.*, Quantum algorithms for electronic structure calculations: Particle-hole Hamiltonian and optimized wave-function expansions, Phys. Rev. A **98**, 022322 (2018).
[62] W. Mizukami, K. Mitarai, Y. O. Nakagawa, T. Yamamoto, T. Yan, and Y. Y. Ohnishi, Orbital optimized unitary coupled cluster theory for quantum computer, Phys. Rev. Res. **2**, 033421 (2020).
[63] N. C. Rubin, J. Lee, and R. Babbush, Compressing many-body fermion operators under unitary constraints, J. Chem. Theory Comput. **18**, 1480 (2022).
[64] J. Cohn, M. Motta, and R. M. Parrish, Quantum filter diagonalization with compressed double-factorized Hamiltonians, PRX Quantum **2**, 040352 (2021).
[65] B. Peng and K. Kowalski, Highly efficient and scalable compound decomposition of two-electron integral tensor and its application in coupled cluster calculations, J. Chem. Theory Comput. **13**, 4179 (2017).
[66] M. Motta, E. Ye, J. R. McClean, Z. Li, A. J. Minnich, R. Babbush, and G. K. Chan, Low rank representations for quantum simulation of electronic structure, npj Quantum Inf. **7**, 83 (2021).
[67] J. Lee, D. W. Berry, C. Gidney, W. J. Huggins, J. R. McClean, N. Wiebe, and R. Babbush, Even more efficient quantum computations of chemistry through tensor hypercontraction, PRX Quantum **2**, 030305 (2021).
[68] https://github.com/sakurairihito/QCMaterialNew.
[69] Y. Suzuki, Y. Kawase, Y. Masumura, Y. Hiraga, M. Nakadai, J. Chen, K. M. Nakanishi, K. Mitarai, R. Imai, S. Tamiya *et al.*, Qulacs: A fast and versatile quantum circuit simulator for research purpose, Quantum **5**, 559 (2021).
[70] J. R. McClean, N. C. Rubin, K. J. Sung, I. D. Kivlichan, X. Bonet-Monroig, Y. Cao, C. Dai, E. S. Fried, C. Gidney, B. Gimby *et al.*, Openfermion: The electronic structure package for quantum computers, Quantum Sci. Technol. **5**, 034014 (2020).
[71] H. Shinaoka, J. Otsuki, M. Kawamura, N. Takemori, and K. Yoshimi, DCore: Integrated DMFT software for correlated electrons, SciPost Phys. **10**, 117 (2021).
[72] https://github.com/BoothGroup/dyson.
[73] L. V. Kantorovich, Mathematical methods of organizing and planning production, Manag. Sci. **6**, 366 (1960).
[74] Markov processes over denumerable products of spaces, describing large systems of automata, Probl. Peredachi Inf. **5** (1969).
[75] N. Gomes, A. Mukherjee, F. Zhang, T. Iadecola, C.-Z. Wang, K.-M. Ho, P. P. Orth, and Y.-X. Yao, Adaptive variational quantum imaginary time evolution approach for ground state preparation, Adv. Quantum Technol. **4**, 2100114 (2021).
[76] D. P. Kingma and J. Ba, Adam: A method for stochastic optimization, arXiv:1412.6980 [cs.LG].
[77] K. M. Nakanishi, K. Fujii, and S. Todo, Sequential minimal optimization for quantum-classical hybrid algorithms, Phys. Rev. Res. **2**, 043158 (2020).
[78] J. Rogers, G. Bhattacharyya, M. S. Frank, T. Jiang, O. Christiansen, Y.-X. Yao, and N. Lanatà, Error mitigation in variational quantum eigensolvers using probabilistic machine learning, arXiv:2111.08814 [quant-ph].
[79] S. Endo, S. C. Benjamin, and Y. Li, Practical quantum error mitigation for near-future applications, Phys. Rev. X **8**, 031027 (2018).
[80] P. Gokhale, O. Angiuli, Y. Ding, K. Gui, T. Tomesh, M. Suchara, M. Martonosi, and F. T. Chong, Minimizing state preparations in variational quantum eigensolver by partitioning into commuting families, arXiv: Quantum Physics (2019) https://api.semanticscholar.org/CorpusID:199000717.
[81] N. Nakatani and G. K.-L. Chan, Efficient tree tensor network states (TTNS) for quantum chemistry: Generalizations of the density matrix renormalization group algorithm, J. Chem. Phys. **138**, 134113 (2013).

[82] G. Carleo and M. Troyer, Solving the quantum many-body problem with artificial neural networks, Science **355**, 602 (2017).

[83] G. Carleo, I. Cirac, K. Cranmer, L. Daudet, M. Schuld, N. Tishby, L. Vogt-Maranto, and L. Zdeborová, Machine learning and the physical sciences, Rev. Mod. Phys. **91**, 045002 (2019).

[84] S. Endo, I. Kurata, and Y. O. Nakagawa, Calculation of the Green's function on near-term quantum computers, Phys. Rev. Res. **2**, 033281 (2020).